Adaptive Finite Element method for reconstructing dielectric properties of malign melanoma in 3D

This article has been accepted for publication in IEEE Open Journal of Antennas and Propagation. This is the author's version which has not been fully edited and content may change prior to final publication. Citation information: DOI 10.1109/OJAP.2026.3714060

IEEE Open Journal of
Antennas and Propagation

Received XX Month, XXXX; revised XX Month, XXXX; accepted XX Month, XXXX; Date of publication XX Month, XXXX; date of current version XX Month, XXXX.

Digital Object Identifier 10.1109/OJAP.2020.1234567

Adaptive Finite Element method for reconstructing dielectric properties of malign melanoma in 3D

Georg Kyhn*, **Larisa Beilina***

[1]Department of Mathematical Sciences, University of Gothenburg, and Chalmers University of Technology, 412 96 Gothenburg Sweden

CORRESPONDING AUTHOR: L. Beilina (e-mail: larisa.beilina@chalmers.se).

This work was supported by the Swedish Research Council grant VR 2024-04459 and STINT grant MG2023-9300.

ABSTRACT The paper presents the performance of an adaptive finite element/finite difference domain decomposition method for reconstructing dielectric permittivity and conductivity functions in a 3D malignant melanoma model using measurements of the backscattered electric field at the boundary of the domain. The inverse problem is formulated as the minimization of a regularized Tikhonov functional, which is solved by constructing the corresponding Lagrangian function. The optimality conditions are obtained from the Fréchet derivative of the Lagrangian. The finite element/finite difference domain decomposition method is formulated, and explicit schemes for solving the forward and adjoint problems are also developed. We present both conjugate gradient and adaptive conjugate gradient reconstruction algorithms to compute a stationary point of the Lagrangian. Numerical experiments are conducted in both homogeneous and non-homogeneous settings with adaptive refinement of the finite element mesh. The computational results demonstrate accurate qualitative and quantitative 3D reconstructions of the weighted dielectric properties of malignant melanoma at 6 GHz.

INDEX TERMS Maxwell's equations; conductive media; microwave imaging; coefficient inverse problem; adaptive finite element method; finite difference method; domain decomposition; Tikhonov functional; Lagrangian approach; conjugate gradient algorithm

I. INTRODUCTION

WITH the global increase in the incidence of malignant melanoma (MM), improving methods for its early detection has become increasingly important [36]. As with most cancers, melanoma is most effectively treated when identified at an early stage [1], [31]. Therefore, the development and promotion of new methods for early detection is essential to reducing mortality from skin cancer, particularly given that MM is the most aggressive form [1]. Recent advances in microwave imaging suggest the potential for developing tools that can support clinical decision-making in melanoma diagnosis, ultimately improving detection outcomes.

In [8], [20], it is shown that MM tissue has different dielectric permittivity and conductivity values from those of the surrounding skin tissue. This suggests that permittivity and conductivity are useful markers for detecting MM tissue.

It is important to emphasize that the prognosis of malignant melanoma is strongly related to the invasion depth of the primary tumor within the skin [13].

In this article, we apply an optimization-based reconstruction algorithm for qualitative and quantitative reconstruction of the weighted relative dielectric permittivity and conductivity functions in three dimensions. This is done using simulated time-dependent backscattered electric field data at the boundary of the investigated domain. One of the most important applications of the studied algorithms is microwave medical imaging.

Microwave biomedical imaging (using electromagnetic waves of frequencies around 1 GHz) has been successfully used for breast cancer screening. In particular, [20] reports different malignant-to-normal tissues contrasts, revealing that malignant tumors have a higher water/liquid content, and thus, higher relative permittivity and conductivity values,

This work is licensed under a Creative Commons Attribution 4.0 License. For more information, see https://creativecommons.org/licenses/by/4.0/

than normal tissues. This observation motivates the development of quantitative algorithms for solving the corresponding coefficient inverse problems (CIPs).

Since the 1990s, quantitative reconstruction algorithms based on the solution of CIPs for Maxwell's system have been developed to provide images of the complex permittivity function. See [11] for 2D techniques, [10], [19] for 3D techniques in the frequency domain and [30], [37] for time domain (TD) techniques. However, in all the above works microwave medical imaging remained largely a research topic and achieved only limited clinical acceptance, [14] since the computations are inefficient, require long processing times, and yield low-contrast images of internal inclusions.

There are two main approaches in microwave medical imaging: microwave tomography [14], [33] and radar-based imaging [21], [22]. In [33] a microwave imaging system was developed in which antennas are arranged in different configurations within a circular array and mounted on a cylindrical chamber filled with various solutions. Another system was developed in [14], [30] for microwave breast imaging. One of the leading groups employing the radar approach in microwave imaging is the research team from the University of Bristol, which has reported clinical tests of a multistatic radar approach [18]. A clinical trial of microwave breast imaging using a mono-static radar-based system was performed in [12].

We begin by presenting the Cauchy formulation of Maxwell's equations restricted to the electric field. The system is then reformulated in a stabilized form to suppress spurious solutions that may arise in numerical implementations. A mathematical analysis of the stabilized Maxwell system is provided in [7], [26]. Based on this stabilized formulation, the inverse problem is posed as an optimization problem for reconstructing two coefficients – dielectric permittivity and conductivity – from backscattered boundary data. This constitutes a CIP, which is inherently ill-posed [15], as the solution does not depend continuously on the input data. Small measurement errors can lead to large variations in the reconstructed coefficients.

To address this issue, we employ Tikhonov regularization within a Lagrangian framework, combined with adaptively refined finite element meshes to reduce reconstruction errors. An a posteriori error indicator was introduced in [6] to guide mesh refinement for the reconstruction of a single parameter in Maxwell's system. In the present work, we extend this approach to enable the simultaneous reconstruction of both dielectric permittivity and conductivity. The objective is then to minimize the Lagrangian and consequently reconstruct the dielectric permittivity and conductivity functions on refined meshes. To this end, we apply an adaptive conjugate gradient algorithm (ACGA) of [24]. The ACGA has been applied to realistic breast phantoms in [5], [6], [25], where the dielectric permittivity function was reconstructed using known values of conductivity. In these studies, the setup was slightly different, with the main distinction being that transmitted data was used in the computations instead of backscattered. The numerical experiments of the current work are performed on simulated backscattered data mimicking a realistic MM growth model in skin at 6 GHz, which was developed in [4]. The present work is an expansion of the ICEAA-IEEE APWC 2025 conference paper [24]. In the paper [24], the authors reconstructed the weighted dielectric properties of MM at 6 GHz placed in a homogeneous domain. In the current paper, we present the reconstruction of weighted dielectric properties of MM in the skin, a significantly more challenging task compared to the reconstruction of MM in a homogeneous domain presented in [24]. Backscattered data from MM in the skin is significantly more complex, as it includes signals not only from the melanoma itself, but also from the epidermis, dermis, and fat. To address this, we employ data preprocessing and calibration procedures. The preprocessing step removes unwanted signal components, isolating those originating solely from the melanoma. Consequently, the backscattered data from the melanoma in the skin becomes more comparable to data from melanoma in a homogeneous domain. We then use the model of melanoma in a homogeneous domain as a reference model for calibrating the preprocessed data. The preprocessed and calibrated data are subsequently used to validate the ACGA reconstruction algorithm. The objective of the numerical experiments is to reconstruct the maximum values of dielectric permittivity and conductivity, as well as their location and shape, in order to identify MM in the skin.

We note that our recent works [24], [27] as well as the current paper use scaled values for the dielectric permittivity and conductivity functions. This simplification is necessary because in our implementation, we apply an adaptive finite element/finite difference domain decomposition method (AFE/FDDDM) [5]. In this approach, finite element and finite difference methods are employed in distinct subdomains. In order to reduce discontinuities between computed solutions in the finite element and the finite difference domains, we use reduced values for dielectric properties of MM. Modifying the finite difference solver to handle realistic values of dielectric properties, particularly for MM, is a planned direction for future research.

The outline of this article is as follows. In Section II, we formulate our forward problem and CIP for Maxwell's equations. We then introduce the regularized Tikhonov functional and the corresponding Lagrangian as well as present the optimality conditions using the Fréchet derivatives of the Lagrangian. Section III introduces the domain decomposition method that solves the forward and adjoint problems, and formulates the ACGA. Section IV presents the data preprocessing procedure used in our numerical simulations. In Section V, we present numerical examples in which the proposed methodology is applied to solve our CIP in both a homogeneous domain and non-homogeneous domain. Lastly, in Section VI, we draw conclusions based on the results.

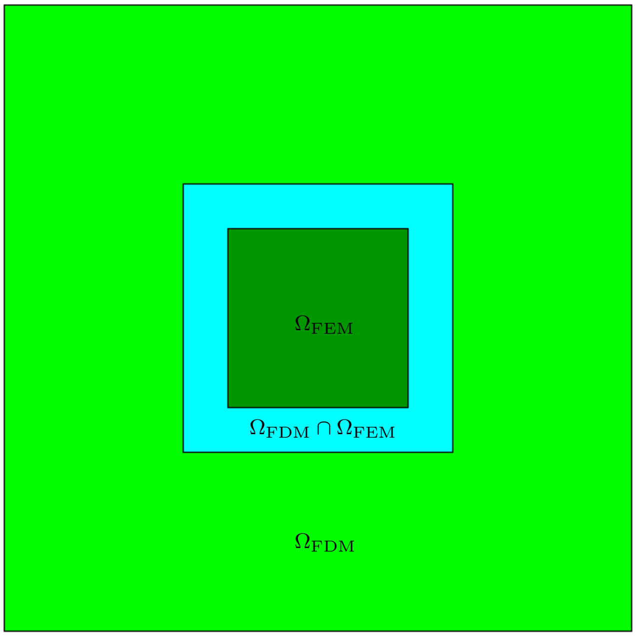

FIGURE 1: A two-dimensional representation of the decomposition of the domain Ω. Here $\Omega = \Omega_{\rm FDM} \cup \Omega_{\rm FEM}$.

II. The mathematical model

This section presents the theoretical foundations of the model problem. We begin by presenting the Cauchy formulation of Maxwell's equations, followed by the stabilized forward problem and the corresponding CIP. The inverse problem is formulated as the minimization of a regularized Tikhonov functional, and the corresponding Lagrangian is introduced to derive the optimality conditions.

A. Formulation of the problem

Let Ω be a bounded, convex domain in $\mathbb{R}^3$ with smooth boundary Γ. The time domain of interest is the interval $(0,T)$ for some end time $T>0$. Define the space-time domains $\Omega_T = \Omega \times (0,T)$ and $\Gamma_T = \Gamma \times (0,T)$.

The model problem considered in this work is formulated solely for the electric field $E\left(x,t\right) = \left(E_1,E_2,E_3\right)\left(x,t\right)$, $x \in \mathbb{R}^3$, satisfying the time-dependent Maxwell's equations in non-magnetic conductive media, under the assumption of zero electric volume charge density:

$$\begin{aligned} \frac{1}{c^2}\varepsilon_r \partial_{tt} E + \nabla\times\nabla\times E &= -\mu_0\sigma\partial_t E, \\ \nabla\cdot(\varepsilon E) &= 0, \\ E(\cdot,0) = f_0, \quad \partial_t E(\cdot,0) &= f_1. \end{aligned} \tag{1}$$

In the model problem (1), the function $\varepsilon_r(x) = \varepsilon(x)/\varepsilon_0$ is the dimensionless relative dielectric permittivity, $\sigma(x)$ is the effective conductivity function, ε_0, μ_0 are the permittivity and permeability of free space, respectively, and $c = 1/\sqrt{\varepsilon_0\mu_0}$ is the speed of light in free space.

Since the multiplicative constants in (1) are small, rounding errors occur. To remedy this, we perform the change of variable $t \to ct$. Note that this change of variable implies that the time interval henceforth becomes $(0, T/c)$. However, since T was chosen arbitrarily, we relabel the new end time T/c as T for simplicity. We also introduce the notation $\sigma := \mu_0 c\sigma$ in order to shorten the notation, and we let $\varepsilon := \varepsilon_r$. Applying this change of variable to (1) yields the following model equation

$$\varepsilon\frac{\partial^2 E}{\partial t^2} + \sigma\frac{\partial E}{\partial t} + \nabla\times(\nabla\times E) = 0 \tag{2}$$

in Ω_T.

In order to use the AFE/FDDDM of [5], the spatial domain Ω is decomposed into subregions $\Omega_{\rm FDM}$ and $\Omega_{\rm FEM}$ such that $\Omega_{\rm FEM}, \Omega_{\rm FDM} \subset \mathbb{R}^3$ where $\Omega = \Omega_{\rm FDM} \cup \Omega_{\rm FEM}$ and $\overline{\Omega}_{\rm FEM} \subset \Omega$ with $\partial\Omega_{\rm FEM} \subset \Omega_{\rm FDM}$, see Fig. 1. Note that $\Gamma \subset \overline{\Omega}_{\rm FDM}$. The finite difference method is applied in $\Omega_{\rm FDM}$, and the finite element method in $\Omega_{\rm FEM}$.

We make the following assumptions on the coefficients:

$$\begin{aligned} \varepsilon \in C_\varepsilon &:= \{\varepsilon \in C^2(\overline{\Omega}) : \varepsilon(x) = 1 \ \forall x \in \Omega_{\rm FDM}, \\ &\qquad \varepsilon(x) \in [1,\overline{\varepsilon}] \ \forall x \in \Omega_{\rm FEM}\} \\ \sigma \in C_\sigma &:= \{\sigma \in C^2(\overline{\Omega}) : \sigma(x) = 0 \ \forall x \in \Omega_{\rm FDM}, \\ &\qquad \sigma(x) \in [0,\overline{\sigma}] \ \forall x \in \Omega_{\rm FEM}\} \end{aligned} \tag{3}$$

where $\overline{\varepsilon} > 1$ and $\overline{\sigma} > 0$ are constants.

Using the assumptions (3) together with the identity

$$\nabla\times(\nabla\times E) = \nabla\nabla\cdot E - \Delta E, \tag{4}$$

in the equation in (2), we obtain the wave equation

$$\frac{\partial^2 E}{\partial t^2} - \Delta E = 0, \tag{5}$$

on $\Omega_{\rm FDM}\times(0,T)$.

We impose the first-order absorbing boundary condition specific to the wave equation (5), as

$$\frac{\partial E}{\partial \mathbf{n}} + \frac{\partial E}{\partial t} = 0,$$

on Γ_T. Here, $\mathbf{n}$ denotes the unit outer normal on Γ and $\frac{\partial E}{\partial \mathbf{n}} = \mathbf{n}\cdot\nabla E$ is the outer normal derivative of the electric field E.

To obtain a numerical solution of (2) with specific initial and boundary conditions, we use a P^1 finite element method (FEM), which can result in spurious solutions [29]. In order to suppress spurious solutions, we introduce the divergence-free condition as a stabilizing term in (2). In [3], it is shown that the introduction of the divergence term into the model equation, when solved with P^1 FEM, removes the spurious solutions for specific values of the dielectric permittivity function. Combining this with the identity (4) gives

$$\varepsilon\frac{\partial^2 E}{\partial t^2} + \sigma\frac{\partial E}{\partial t} - \Delta E - \nabla\nabla\cdot\left(\left(\varepsilon - 1\right)E\right) = 0.$$

Let $H^p(\Omega_T)$ denote the usual Sobolev space of order $p \in \{1,2\}$, and let $f_0, f_1 \in \left[H^2(\Omega)\right]^3$ denote the initial conditions. Then the forward problem and the inverse problem can be stated as follows.

Forward problem: Let $\varepsilon \in C_\varepsilon$, $\sigma \in C_\sigma$, and $f_0, f_1 \in \left[H^2(\Omega)\right]^3$, find $E \in \left[H^2(\Omega_T)\right]^3$ such that

$$\varepsilon \frac{\partial^2 E}{\partial t^2} + \sigma \frac{\partial E}{\partial t} - \Delta E - \nabla\nabla \cdot ((\varepsilon - 1) E) = 0, \quad \text{in } \Omega_T, \tag{6a}$$

$$E(\cdot, 0) = f_0, \quad \text{in } \Omega, \tag{6b}$$

$$\frac{\partial E}{\partial t}(\cdot, 0) = f_1, \quad \text{in } \Omega, \tag{6c}$$

$$\frac{\partial E}{\partial \mathbf{n}} + \frac{\partial E}{\partial t} = 0, \quad \text{on } \Gamma_T. \tag{6d}$$

This problem is well posed; see [7], [26] as well as references therein. Let $E_{\text{obs}} \in \left[L^2(\Gamma_T)\right]^3$ be the observations made on the boundary Γ_T, we can state the inverse problem.

Inverse problem: Suppose that an exact solution of the problem (6) exists, E^*, for the exact functions $(\varepsilon^*, \sigma^*)$. Let the function E_{obs} be such that

$$E_{\text{obs}}(x,t) = E^*(x,t,\varepsilon^*,\sigma^*)|_{\Gamma_T} + E_\delta(x,t), \quad (x,t) \in \Gamma_T,$$

where the function $E_\delta(x,t)$ denotes the measurement error satisfying

$$\|E_\delta(x,t)\|_{\Gamma_T} \leq \delta.$$

Find $\varepsilon \in C_\varepsilon$ and $\sigma \in C_\sigma$ for observations E_{obs} on Γ_T.

It is well known that the CIP for Maxwell's equations is an ill-posed problem, see [28, Section 3]. In this article, we adopt an optimization-based approach, similar to that employed in [5], [6], [24], [25].

B. The Tikhonov functional and the Lagrangian

To solve the inverse problem, we introduce a regularized Tikhonov functional J, which we aim to minimize. The minimization problem is solved using a Lagrangian approach subject to the constraint that the electric field satisfies (6a). Optimality conditions are derived using the Fréchet derivatives of the Lagrangian, leading to the formulation of an associated adjoint problem.

We first introduce the following function spaces. For $p \in \{1, 2\}$, let

$$\begin{aligned} H_E^p(\Omega_T) &= \Big\{ v \in [H^p(\Omega_T)]^3 : v(\cdot,0) = f_0, \\ &\qquad \frac{\partial v}{\partial t}(\cdot,0) = f_1 \Big\}, \\ H_0^p(\Omega_T) &= \left\{ v \in [H^p(\Omega_T)]^3 : v(\cdot,0) = \frac{\partial v}{\partial t}(\cdot,0) = 0 \right\}, \\ H_\lambda^p(\Omega_T) &= \left\{ v \in [H^p(\Omega_T)]^3 : v(\cdot,T) = \frac{\partial v}{\partial t}(\cdot,T) = 0 \right\}. \end{aligned}$$

Next, we introduce the Tikhonov functional defined by

$$\begin{aligned} J(E,\varepsilon,\sigma) &= \frac{1}{2} \int_0^T \int_\Gamma |E - E_{\text{obs}}|^2 \, \mathrm{d}s\mathrm{d}t \\ &\quad + \frac{\gamma_\varepsilon}{2} \int_\Omega (\varepsilon - \varepsilon^0)^2 \mathrm{d}x + \frac{\gamma_\sigma}{2} \int_\Omega (\sigma - \sigma^0)^2 \mathrm{d}x. \end{aligned} \tag{7}$$

Here, $E_{\text{obs}} \in \left[L^2(\Gamma_T)\right]^3$ is the observed electric field, $\gamma_\varepsilon, \gamma_\sigma \in \mathbb{R}$ are the regularization parameters, ε^0 and σ^0 are initial guesses for ε and σ, respectively. The latter two terms of (7) are regularization terms that penalize deviations of ε and σ from their initial guesses. We define the minimization problem as

$$\min_{\varepsilon,\sigma} J(E,\varepsilon,\sigma), \tag{8}$$

where $\varepsilon \in C_\varepsilon$, $\sigma \in C_\sigma$, and E solves (6).

To solve the minimization problem (8), we assume that $E \in [H^2(\Omega_T)]^3$ satisfies (6). We then use (6a) as a constraint and introduce the Lagrangian, $\mathcal{L}$, in strong form as

$$\begin{aligned} \mathcal{L}(E,\lambda,\varepsilon,\sigma) &= J(E,\varepsilon,\sigma) + \int_0^T \int_\Omega \lambda \Big(\varepsilon \frac{\partial^2 E}{\partial t^2} \\ &\quad + \sigma \frac{\partial E}{\partial t} - \Delta E - \nabla\nabla \cdot ((\varepsilon - 1) E) \Big) \mathrm{d}x\mathrm{d}t. \end{aligned} \tag{9}$$

Here, $\lambda \in H_\lambda^2(\Omega_T)$ is the Lagrange multiplier, and we restrict $E \in H_E^2(\Omega_T)$, where the initial conditions (6b) and (6c) are imposed[1].

Because the finite element method is employed later to solve the CIP, the Lagrangian must be formulated in weak form. The weak formulation of the Lagrangian given in (9) is:

$$\begin{aligned} \mathcal{L}(E,\lambda,\varepsilon,\sigma) &= \frac{1}{2} \int_0^T \int_\Gamma |E - E_{\text{obs}}|^2 \, \mathrm{d}s\mathrm{d}t \\ &\quad + \frac{\gamma_\varepsilon}{2} \int_\Omega (\varepsilon - \varepsilon^0)^2 \mathrm{d}x + \frac{\gamma_\sigma}{2} \int_\Omega (\sigma - \sigma^0)^2 \mathrm{d}x \\ &\quad - \int_\Omega \varepsilon(x)\lambda(x,0) f_1(x) \mathrm{d}x \\ &\quad - \int_\Omega \varepsilon \int_0^T \frac{\partial \lambda}{\partial t} \frac{\partial E}{\partial t} \mathrm{d}t\mathrm{d}x \\ &\quad - \int_\Omega \sigma(x)\lambda(x,0) f_0(x) \mathrm{d}x \\ &\quad - \int_\Omega \sigma \int_0^T \frac{\partial \lambda}{\partial t} E \mathrm{d}t\mathrm{d}x \\ &\quad + \int_0^T \int_\Gamma \lambda \frac{\partial E}{\partial t} \mathrm{d}s\mathrm{d}t + \int_0^T \int_\Omega \nabla\lambda \nabla E \mathrm{d}x\mathrm{d}t \\ &\quad + \int_0^T \int_\Omega \nabla \cdot \lambda \nabla \cdot ((\varepsilon - 1) E) \, \mathrm{d}x\mathrm{d}t. \end{aligned}$$

Next, we define the domain $\mathcal{U}$ of the variational formulation of the Lagrangian, and the set $\mathcal{U}^0$ as

$$\begin{aligned} \mathcal{U} &= H_E^1(\Omega_T) \times H_\lambda^1(\Omega_T) \times C_\varepsilon \times C_\sigma, \\ \mathcal{U}^0 &= H_0^1(\Omega_T) \times H_\lambda^1(\Omega_T) \times C_\varepsilon \times C_\sigma, \end{aligned}$$

[1] Note that (6d) is still assumed to hold for E.

This article has been accepted for publication in IEEE Open Journal of Antennas and Propagation. This is the author's version which has not been fully edited and content may change prior to final publication. Citation information: DOI 10.1109/OJAP.2026.3714060

such that $\mathcal{L} : \mathcal{U} \to \mathbb{R}$.

Then, to solve (8), we need to find a stationary point $u = (E, \lambda, \varepsilon, \sigma) \in \mathcal{U}$ of the Lagrangian, such that

$$D\mathcal{L}(u; \tilde{u}) = 0 \tag{10}$$

for all $\tilde{u} \in \mathcal{U}^0$. Here,

$$\begin{aligned} &D\mathcal{L}(u; \tilde{u}) \\ &\quad = \left(\partial_E \mathcal{L}(u; \tilde{E}), \partial_\lambda \mathcal{L}(u; \tilde{\lambda}), \partial_\varepsilon \mathcal{L}(u; \tilde{\varepsilon}), \partial_\sigma \mathcal{L}(u; \tilde{\sigma})\right) \end{aligned}$$

is the Fréchet derivative of $\mathcal{L}$ at u in the direction of $\tilde{u} = \left(\tilde{E}, \tilde{\lambda}, \tilde{\varepsilon}, \tilde{\sigma}\right)$.

The optimality condition (10) is equivalent to the following four optimality conditions: find $u \in \mathcal{U}$ such that

$$\begin{aligned} 0 &= \partial_E \mathcal{L}(u; \tilde{E}) \\ &= \int_0^T \int_\Gamma (E - E_{\text{obs}}) \tilde{E} \mathrm{d}s\mathrm{d}t - \int_\Omega \varepsilon \int_0^T \frac{\partial \lambda}{\partial t} \frac{\partial \tilde{E}}{\partial t} \mathrm{d}t\mathrm{d}x \\ &\quad - \int_\Omega \sigma \int_0^T \frac{\partial \lambda}{\partial t} \tilde{E} \mathrm{d}t\mathrm{d}x + \int_0^T \int_\Gamma \lambda \frac{\partial \tilde{E}}{\partial t} \mathrm{d}s\mathrm{d}t \\ &\quad + \int_0^T \int_\Omega \nabla \lambda \nabla \tilde{E} \mathrm{d}x\mathrm{d}t \\ &\quad + \int_0^T \int_\Omega \nabla \cdot \lambda \nabla \cdot \left((\varepsilon - 1)\, \tilde{E}\right) \mathrm{d}x\mathrm{d}t, \end{aligned} \tag{11}$$

$$\begin{aligned} 0 &= \partial_\lambda \mathcal{L}(u; \tilde{\lambda}) \\ &= -\int_\Omega \varepsilon(x) \tilde{\lambda}(x, 0) f_1(x) \mathrm{d}x - \int_\Omega \varepsilon \int_0^T \frac{\partial \tilde{\lambda}}{\partial t} \frac{\partial E}{\partial t} \mathrm{d}t\mathrm{d}x \\ &\quad - \int_\Omega \sigma(x) \tilde{\lambda}(x, 0) f_0(x) \mathrm{d}x - \int_\Omega \sigma \int_0^T \frac{\partial \tilde{\lambda}}{\partial t} E \mathrm{d}t\mathrm{d}x \\ &\quad + \int_0^T \int_\Gamma \tilde{\lambda} \frac{\partial E}{\partial t} \mathrm{d}s\mathrm{d}t + \int_0^T \int_\Omega \nabla \tilde{\lambda} \nabla E \mathrm{d}x\mathrm{d}t \\ &\quad + \int_0^T \int_\Omega \nabla \cdot \tilde{\lambda} \nabla \cdot ((\varepsilon - 1)\, E) \mathrm{d}x\mathrm{d}t, \end{aligned} \tag{12}$$

$$\begin{aligned} 0 &= \partial_\varepsilon \mathcal{L}(u; \tilde{\varepsilon}) \\ &= \gamma_\varepsilon \int_\Omega (\varepsilon - \varepsilon^0) \tilde{\varepsilon} \mathrm{d}x - \int_\Omega \tilde{\varepsilon}(x) \lambda(x, 0) f_1(x) \mathrm{d}x \\ &\quad - \int_\Omega \tilde{\varepsilon} \int_0^T \frac{\partial \lambda}{\partial t} \frac{\partial E}{\partial t} \mathrm{d}t\mathrm{d}x + \int_0^T \int_\Omega \nabla \cdot \lambda \nabla \cdot \tilde{\varepsilon} E \mathrm{d}x\mathrm{d}t, \end{aligned} \tag{13}$$

$$\begin{aligned} 0 &= \partial_\sigma \mathcal{L}(u; \tilde{\sigma}) \\ &= \gamma_\sigma \int_\Omega (\sigma - \sigma^0) \tilde{\sigma} \mathrm{d}x - \int_\Omega \tilde{\sigma}(x) \lambda(x, 0) f_0(x) \mathrm{d}x \\ &\quad - \int_\Omega \tilde{\sigma} \int_0^T \frac{\partial \lambda}{\partial t} E \mathrm{d}t\mathrm{d}x, \end{aligned} \tag{14}$$

which hold for all $\tilde{E} \in H_0^1(\Omega_T)$, $\tilde{\lambda} \in H_\lambda^1(\Omega_T)$, $\tilde{\varepsilon} \in C_\varepsilon$ and $\tilde{\sigma} \in C_\sigma$.

By applying integration by parts in space to the optimality conditions (11) and (12), we derive the adjoint problem and the forward problem, respectively.

Adjoint problem: Find $\lambda \in \left[H^2(\Omega_T)\right]^3$ such that

$$\varepsilon \frac{\partial^2 \lambda}{\partial t^2} - \sigma \frac{\partial \lambda}{\partial t} - \Delta \lambda - (\varepsilon - 1) \nabla \nabla \cdot \lambda = 0, \quad \text{in } \Omega_T, \tag{15a}$$

$$\lambda(\cdot, T) = \frac{\partial \lambda}{\partial t}(\cdot, T) = 0, \quad \text{in } \Omega, \tag{15b}$$

$$\frac{\partial \lambda}{\partial \mathbf{n}} = \frac{\partial \lambda}{\partial t} - (E - E_{\text{obs}}), \quad \text{on } \Gamma_T, \tag{15c}$$

for given functions $E, E_{\text{obs}} \in \left[L^2(\Omega_T)\right]^3$, $\varepsilon \in C_\varepsilon$, and $\sigma \in C_\sigma$.

III. Domain Decomposition method

We formulate our problem in the framework of the domain decomposition method, since all our computations use the AFE/FDDDM developed in [5].

Let us now define a partition of Ω_{FEM} and the time interval $(0, T)$, before stating the forward problem (6) and the adjoint problem (15) on $\Omega_{\text{FEM}_T} = \Omega_{\text{FEM}} \times (0, T)$. Let $\mathbb{K}_h$ be a partition of the FE domain Ω_{FEM} consisting of tetrahedra satisfying the regularity condition in [9], [23], such that

$$\mathbb{K}_h = \bigcup_{\ell=1}^{L} K_\ell,$$

where L is the number of elements K_ℓ. Here, $h = h(x)$ is a piecewise constant mesh function such that

$$h(x) = h_{K_\ell} \qquad \text{for } x \in K_\ell, \text{ for all } \ell \in \{1, \ldots, L\},$$

and represents the diameter of each mesh element. Let $\partial\mathbb{K}_h$ denote the partition of the boundary $\partial\Omega_{\text{FEM}}$ into the boundaries ∂K_ℓ of those elements K_ℓ having vertices on $\partial\Omega_{\text{FEM}}$. We partition the time interval $[0, T]$ as follows: Let $N \in \mathbb{N}$ be the number of time steps, and let $\tau = T/N$ be the uniform mesh size. Let $t_k \in [0, T]$ be the k-th time level such that $t_k = \tau k$ for all $k \in \{0, \ldots, N\}$. Let us now formulate the forward and adjoint problems within the AFE/FDDDM framework.

Forward FEM problem in AFE/FDDDM: Find $E_{\mathrm{FE}} \in \left[H^2(\Omega_{\mathrm{FEM}_T})\right]^3$ such that

$$\varepsilon \frac{\partial^2 E_{\mathrm{FE}}}{\partial t^2} + \sigma \frac{\partial E_{\mathrm{FE}}}{\partial t} - \Delta E_{\mathrm{FE}} - \nabla\nabla \cdot ((\varepsilon - 1) E_{\mathrm{FE}}) = 0, \quad \text{in } \Omega_{\mathrm{FEM}_T}, \tag{16a}$$

$$E_{\mathrm{FE}}(\cdot, 0) = f_0, \quad \text{in } \Omega_{\mathrm{FEM}}, \tag{16b}$$

$$\frac{\partial E_{\mathrm{FE}}}{\partial t}(\cdot, 0) = f_1, \quad \text{in } \Omega_{\mathrm{FEM}}, \tag{16c}$$

$$\frac{\partial E_{\mathrm{FE}}}{\partial \mathbf{n}} = \frac{\partial E_{\mathrm{FD}}}{\partial \mathbf{n}}, \quad \text{on } \partial\Omega_{\mathrm{FEM}_T}, \tag{16d}$$

for given functions $\varepsilon \in C_\varepsilon$, $\sigma \in C_\sigma$, and $f_0, f_1 \in \left[H^2(\Omega)\right]^3$.

Forward FDM problem in AFE/FDDDM: Find $E_{\mathrm{FD}} \in \left[H^2(\Omega_{\mathrm{FDM}_T})\right]^3$ such that

$$\frac{\partial^2 E_{\mathrm{FD}}}{\partial t^2} - \Delta E_{\mathrm{FD}} = 0, \quad \text{in } \Omega_{\mathrm{FDM}_T}, \tag{17a}$$

$$E_{\mathrm{FD}}(\cdot, 0) = f_0, \quad \text{in } \Omega_{\mathrm{FDM}}, \tag{17b}$$

$$\frac{\partial E_{\mathrm{FD}}}{\partial t}(\cdot, 0) = f_1, \quad \text{in } \Omega_{\mathrm{FDM}}, \tag{17c}$$

$$\frac{\partial E_{\mathrm{FD}}}{\partial \mathbf{n}} = \frac{\partial E_{\mathrm{FE}}}{\partial \mathbf{n}}, \quad \text{on } \partial\Omega_{\mathrm{FDM}_T} \cap \Omega_{\mathrm{FEM}_T}, \tag{17d}$$

$$\frac{\partial E_{\mathrm{FD}}}{\partial \mathbf{n}} + \frac{\partial E_{\mathrm{FD}}}{\partial t} = 0, \quad \text{on } \Gamma_T \cap \Omega_{\mathrm{FDM}_T}, \tag{17e}$$

for given functions $f_0, f_1 \in \left[H^2(\Omega)\right]^3$.

Lemma 1:
Given $\varepsilon \in C_\varepsilon$, $\sigma \in C_\sigma$, and $f_0, f_1 \in \left[H^2(\Omega)\right]^3$, let E_{FE} and E_{FD} be the solutions to (16) and (17), respectively. Set

$$E = \begin{cases} E_{\mathrm{FE}} & \text{on } \Omega_{\mathrm{FEM}_T}, \\ E_{\mathrm{FD}} & \text{on } \Omega_{\mathrm{FDM}_T} \backslash \Omega_{\mathrm{FEM}_T}. \end{cases}$$

Then E solves (6).

See [7] and the references therein for a proof.

In order to discretize the forward and adjoint problems, we need to define finite-dimensional subspaces of the test space. To do this, let

$$V_h(\Omega_{\mathrm{FEM}}) = \left\{ v \in H^1(\Omega_{\mathrm{FEM}}) : v|_{K_\ell} \in P^1(K_\ell), \ \text{for all } \ell \in \{0, \dots, L\} \right\},$$

where $P^1(K_\ell)$ is the set of piecewise linear functions over K_ℓ.

Lemma 2:
The explicit finite element scheme for (16) with $E = E_{\mathrm{FE}}$ is: Given $\varepsilon_h, \sigma_h \in V_h(\Omega_{\mathrm{FEM}})$ and $f_{0h}, f_{1h} \in \left[V_h(\Omega_{\mathrm{FEM}})\right]^3$ find a sequence $\{E_h^k\}_{k=0}^N \subset \left[V_h(\Omega_{\mathrm{FEM}})\right]^3$ such that

$$\begin{aligned} E_h^0 &= f_{0h}, \\ E_h^1 &= E_h^0 + \tau f_{1h}, \\ \int_{\Omega_{\mathrm{FEM}}} & (2\varepsilon_h + \tau\sigma_h) E_h^{k+1} v_h \mathrm{d}x \\ &= 4 \int_{\Omega_{\mathrm{FEM}}} \varepsilon_h E_h^k v_h \mathrm{d}x \\ &\quad - 2\tau^2 \int_{\Omega_{\mathrm{FEM}}} \nabla E_h^k \nabla v_h \mathrm{d}x \\ &\quad - 2\tau^2 \int_{\Omega_{\mathrm{FEM}}} \nabla \cdot ((\varepsilon_h - 1) E_h^k) \nabla \cdot v_h \mathrm{d}x \\ &\quad - \int_{\Omega_{\mathrm{FEM}}} (2\varepsilon_h - \tau\sigma_h) E_h^{k-1} v_h \mathrm{d}x \\ &\quad + 2\tau^2 \int_{\partial\Omega_{\mathrm{FEM}}} \frac{\partial E_{\mathrm{FD}_h}^k}{\partial \mathbf{n}} v_h \mathrm{d}s, \end{aligned}$$

for all $v_h \in \left[V_h(\Omega_{\mathrm{FEM}})\right]^3$.

Proof:
Multiplying (16a) by a test function $v \in H_0^1(\Omega_{\mathrm{FEM}})$, integrating over Ω_{FEM} and performing integration by parts in space, we get the following expression

$$\begin{aligned} 0 = &\int_{\Omega_{\mathrm{FEM}}} \varepsilon \frac{\partial^2 E}{\partial t^2} v \mathrm{d}x + \int_{\Omega_{\mathrm{FEM}}} \sigma \frac{\partial E}{\partial t} v \mathrm{d}x \\ &- \int_{\partial\Omega_{\mathrm{FEM}}} \frac{\partial E_{\mathrm{FD}}}{\partial \mathbf{n}} v \mathrm{d}s + \int_{\Omega_{\mathrm{FEM}}} \nabla E \nabla v \mathrm{d}x \\ &+ \int_{\Omega_{\mathrm{FEM}}} \nabla \cdot ((\varepsilon - 1) E) \nabla \cdot v \mathrm{d}x. \end{aligned} \tag{18}$$

In order to obtain a time-discrete scheme in Ω_{FEM_T}, we apply finite difference (FD) approximations of the time derivatives. We define $E_h^k(x) \in \left[V_h(\Omega_{\mathrm{FEM}})\right]^3$ as the FEM approximation of $E^k(x) = E(x, t_k)$ for all $k \in \{0, \dots, N\}$, where $t_k = \tau k$ as previously defined. Applying FD approximations to the time derivatives in (18) and evaluating the resulting equation at $t = t_k$ yields

$$\begin{aligned} 0 = &\int_{\Omega_{\mathrm{FEM}}} \varepsilon_h \left(\frac{E_h^{k+1} - 2E_h^k + E_h^{k-1}}{\tau^2} \right) v_h \mathrm{d}x \\ &+ \int_{\Omega_{\mathrm{FEM}}} \sigma_h \left(\frac{E_h^{k+1} - E_h^{k-1}}{2\tau} \right) v_h \mathrm{d}x \\ &- \int_{\partial\Omega_{\mathrm{FEM}}} \frac{\partial E_{\mathrm{FD}_h}^k}{\partial \mathbf{n}} v_h \mathrm{d}s \\ &+ \int_{\Omega_{\mathrm{FEM}}} \nabla E_h^k \nabla v_h \mathrm{d}x \\ &+ \int_{\Omega_{\mathrm{FEM}}} \nabla \cdot ((\varepsilon_h - 1) E_h^k) \nabla \cdot v_h \mathrm{d}x, \end{aligned} \tag{19}$$

for $k \in \{1,\ldots,N-1\}$. Multiplying both sides of (19) by $2\tau^2$ and rearranging the terms, we get

$$\begin{aligned}\int_{\Omega_{\mathrm{FEM}}} &(2\varepsilon_h + \tau\sigma_h)\, E_h^{k+1} v_h \mathrm{d}x \\ &= 4\int_{\Omega_{\mathrm{FEM}}} \varepsilon_h E_h^k v_h \mathrm{d}x \\ &\quad - 2\tau^2 \int_{\Omega_{\mathrm{FEM}}} \nabla E_h^k \nabla v_h \mathrm{d}x \\ &\quad - 2\tau^2 \int_{\Omega_{\mathrm{FEM}}} \nabla\cdot((\varepsilon_h - 1)E_h^k)\nabla\cdot v_h \mathrm{d}x \\ &\quad - \int_{\Omega_{\mathrm{FEM}}} (2\varepsilon_h - \tau\sigma_h)\, E_h^{k-1} v_h \mathrm{d}x \\ &\quad + 2\tau^2 \int_{\partial\Omega_{\mathrm{FEM}}} \frac{\partial E_{\mathrm{FD}_h}^k}{\partial \mathbf{n}} v_h \mathrm{d}s.\end{aligned}$$

Since $f_{0h} = E_h(\cdot,0) = E_h^0$ and $f_{1h} = \frac{\partial E_h}{\partial t}(\cdot,0) \approx \frac{E_h^1 - E_h^0}{\tau}$ by the FD approximation, where f_{0h} and f_{1h} are the $[V_h(\Omega_{\mathrm{FEM}})]^3$ projections of f_0 and f_1, respectively, rearranging these terms gives $E_h^1 = E_h^0 + \tau f_{1h}$. The result then follows. ■

Details of the derivation of the explicit FE scheme can be found in [5]. An analogous result holds for the adjoint problem (15).

Adjoint FEM problem in AFE/FDDDM: Find $\lambda_{\mathrm{FE}} \in \left[H^2(\Omega_{\mathrm{FEM}_T})\right]^3$ such that

$$\varepsilon \frac{\partial^2 \lambda_{\mathrm{FE}}}{\partial t^2} - \sigma \frac{\partial \lambda_{\mathrm{FE}}}{\partial t} - \Delta\lambda_{\mathrm{FE}} - (\varepsilon - 1)\nabla\nabla\cdot\lambda_{\mathrm{FE}} = 0, \quad \text{in } \Omega_{\mathrm{FEM}_T}, \tag{20a}$$

$$\lambda_{\mathrm{FE}}(\cdot,T) = \frac{\partial \lambda_{\mathrm{FE}}}{\partial t}(\cdot,T) = 0, \quad \text{in } \Omega_{\mathrm{FEM}}, \tag{20b}$$

$$\frac{\partial \lambda_{\mathrm{FE}}}{\partial \mathbf{n}} = \frac{\partial \lambda_{\mathrm{FD}}}{\partial \mathbf{n}}, \quad \text{on } \partial\Omega_{\mathrm{FEM}_T}, \tag{20c}$$

for given functions $\varepsilon \in C_\varepsilon$, $\sigma \in C_\sigma$, and $\lambda_{\mathrm{FD}} \in \left[H^2(\Omega_{\mathrm{FDM}_T})\right]^3$.

Adjoint FDM problem in AFE/FDDDM: Find $\lambda_{\mathrm{FD}} \in \left[H^2(\Omega_{\mathrm{FDM}_T})\right]^3$ such that

$$\frac{\partial^2 \lambda_{\mathrm{FD}}}{\partial t^2} - \Delta\lambda_{\mathrm{FD}} = 0, \quad \text{in } \Omega_{\mathrm{FDM}_T}, \tag{21a}$$

$$\lambda_{\mathrm{FD}}(x,T) = \frac{\partial \lambda_{\mathrm{FD}}}{\partial t}(x,T) = 0, \quad \text{in } \Omega_{\mathrm{FDM}}, \tag{21b}$$

$$\frac{\partial \lambda_{\mathrm{FD}}}{\partial \mathbf{n}} = \frac{\partial \lambda_{\mathrm{FE}}}{\partial \mathbf{n}}, \quad \text{on } \partial\Omega_{\mathrm{FDM}_T} \cap \Omega_{\mathrm{FEM}_T}, \tag{21c}$$

$$\frac{\partial \lambda_{\mathrm{FD}}}{\partial \mathbf{n}} = \frac{\partial \lambda_{\mathrm{FD}}}{\partial t} - (E - E_{\mathrm{obs}}), \quad \text{on } \Gamma_T \cap \Omega_{\mathrm{FDM}_T}, \tag{21d}$$

for given functions $E, E_{\mathrm{obs}} \in \left[L^2(\Gamma_T)\right]^3$, and $\lambda_{\mathrm{FE}} \in \left[H^2(\Omega_{\mathrm{FEM}_T})\right]^3$.

Lemma 3:
Let $E, E_{\mathrm{obs}} \in \left[L^2(\Gamma_T)\right]^3$ be the forward solution and the observed electric field, respectively, as well as $\varepsilon \in C_\varepsilon$ and $\sigma \in C_\sigma$. Further, let λ_{FE} and λ_{FD} be the solutions to (20) and (21), respectively, and set

$$\lambda = \begin{cases} \lambda_{\mathrm{FE}} & \text{on } \Omega_{\mathrm{FEM}_T}, \\ \lambda_{\mathrm{FD}} & \text{on } \Omega_{\mathrm{FDM}_T} \backslash \Omega_{\mathrm{FEM}_T}. \end{cases}$$

Then λ solves (15).

See [7] for proof.

Lemma 4:
The FEM formulation of (20) with $\lambda = \lambda_{\mathrm{FE}}$ is: Given $\varepsilon_h, \sigma_h \in V_h(\Omega_{\mathrm{FEM}})$, find a sequence $\{\lambda_h^k\}_{k=N}^0 \subset [V_h(\Omega_{\mathrm{FEM}})]^3$ such that

$$\begin{aligned}&\lambda_h^N = \lambda_h^{N-1} = 0, \\ &\int_{\Omega_{\mathrm{FEM}}} (2\varepsilon_h + \tau\sigma_h)\lambda_h^{k-1} v_h \mathrm{d}x \\ &\quad = 4\int_{\Omega_{\mathrm{FEM}}} \varepsilon_h \lambda_h^k v_h \mathrm{d}x \\ &\qquad - 2\tau^2 \int_{\Omega_{\mathrm{FEM}}} \nabla\lambda_h^k \nabla v_h \mathrm{d}x \\ &\qquad - 2\tau^2 \int_{\Omega_{\mathrm{FEM}}} \nabla\cdot\lambda_h^k \nabla\cdot((\varepsilon_h - 1)v_h)\mathrm{d}x \\ &\qquad - \int_{\Omega_{\mathrm{FEM}}} (2\varepsilon_h - \tau\sigma_h)\, \lambda_h^{k+1} v_h \mathrm{d}x \\ &\qquad + 2\tau^2 \int_{\partial\Omega_{\mathrm{FEM}}} \frac{\partial \lambda_{\mathrm{FD}_h}^k}{\partial \mathbf{n}} v_h \mathrm{d}x,\end{aligned}$$

for all $v_h \in [V_h(\Omega_{\mathrm{FEM}})]^3$.

Proof:

Proceeding as in the proof of Lemma 2, we define $\lambda_h^k \in [V_h(\Omega_{\mathrm{FEM}})]^3$ as the FEM approximation of $\lambda^k(x) = \lambda(x, t_k)$ for all $k \in \{0, \dots, N\}$ and apply FDM in time to (20). This gives

$$\begin{aligned} \int_{\partial\Omega_{\mathrm{FEM}}} & \frac{\partial \lambda^k_{\mathrm{FD}_h}}{\partial \mathbf{n}} v_h \mathrm{d}x \\ &= \int_{\Omega_{\mathrm{FEM}}} \varepsilon_h \left(\frac{\lambda_h^{k+1} - 2\lambda_h^k + \lambda_h^{k-1}}{\tau^2} \right) v_h \mathrm{d}x \\ &\quad - \int_{\Omega_{\mathrm{FEM}}} \sigma_h \left(\frac{\lambda_h^{k+1} - \lambda_h^{k-1}}{2\tau} \right) v_h \mathrm{d}x \\ &\quad + \int_{\Omega_{\mathrm{FEM}}} \nabla \lambda_h^k \nabla v_h \mathrm{d}x \\ &\quad + \int_{\Omega_{\mathrm{FEM}}} \nabla \cdot \lambda_h^k \nabla \cdot ((\varepsilon_h - 1) v_h) \mathrm{d}x. \end{aligned} \tag{22}$$

Here, $\lambda^k_{\mathrm{FD}_h}$ denotes the FEM approximation of $\lambda_{\mathrm{FD}}(x, t_k)$, where λ_{FD} solves (21). Multiplying (22) by $2\tau^2$ and rearranging the terms yields an explicit expression of λ_h^{k-1} in terms of the subsequent time steps λ_h^k and λ_h^{k+1}. Observing that $0 = \frac{\partial \lambda_h}{\partial t}(\cdot, T) \approx \frac{\lambda_h^N - \lambda_h^{N-1}}{\tau}$ together with $0 = \lambda_h(\cdot, T) = \lambda_h^N$ implies that $\lambda_h^{N-1} = 0$. The result then follows. ∎

For details on applying AFE/FDDDM for the numerical solution of forward and adjoint problems, see [5]. We now have the necessary tools to solve both the forward and adjoint problems, and we turn our attention to the remaining optimality conditions, (13) and (14). These conditions are used in the iterative gradient update of the dielectric permittivity and conductivity functions in both the CGA and the ACGA.

A. Gradient methods

In this section, we introduce the conjugate gradient algorithm (CGA) and the adaptive conjugate gradient algorithm (ACGA). The conjugate gradient method minimize the Tikhonov functional (7), thereby solving the inverse problem.

Solving the inverse problem amounts to finding a solution of the optimality conditions (13) and (14). We define the gradients $g_\varepsilon : \Omega \to \mathbb{R}$ and $g_\sigma : \Omega \to \mathbb{R}$ such that

$$\begin{aligned} g_\varepsilon(x) = \Bigg[& \gamma_\varepsilon(\varepsilon - \varepsilon^0) - \lambda(\cdot, 0) f_1 - \int_0^T \frac{\partial \lambda}{\partial t} \frac{\partial E}{\partial t} \mathrm{d}t \\ & + \int_0^T \nabla \cdot \lambda \nabla \cdot E \mathrm{d}t \Bigg](x), \end{aligned} \tag{23}$$

$$g_\sigma(x) = \left[\gamma_\sigma(\sigma - \sigma^0) - \lambda(\cdot, 0) f_0 - \int_0^T \frac{\partial \lambda}{\partial t} E \mathrm{d}t \right](x). \tag{24}$$

Then $\int_\Omega g_\varepsilon \tilde{\varepsilon} \mathrm{d}x = \partial_\varepsilon \mathcal{L}(u; \tilde{\varepsilon})$ and $\int_\Omega g_\sigma \tilde{\sigma} \mathrm{d}x = \partial_\sigma \mathcal{L}(u; \tilde{\sigma})$ for all $\tilde{\varepsilon} \in C_\varepsilon$ and $\tilde{\sigma} \in C_\sigma$. Here, we assume that $(\nabla \tilde{\varepsilon})E = 0$. Applying the chain rule, we obtain $\nabla \cdot \tilde{\varepsilon} E = (\nabla \tilde{\varepsilon})E + \tilde{\varepsilon} \nabla \cdot E = \tilde{\varepsilon} \nabla \cdot E$. Utilizing (23) and (24), we formulate the CGA as Algorithm 1.

To further improve the reconstruction results obtained by the CGA, mesh refinement is incorporated, leading to the formulation of the ACGA, see Algorithm 2. Details of the AFE/FDDDM and ACGA can be found in [5], [25]. This algorithm refines the mesh only in space and not in time in order to ensure the efficient execution of the adaptive finite element/finite difference method.

Algorithm 1: Conjugate Gradient Algorithm (CGA): For iterations $m = 0, \dots, M$ perform the following steps.

1. Initialization: set $m = 0$ and choose initial guesses ε^0, σ^0, γ_ε^0, and γ_σ^0.
2. Calculate E^m, λ^m, g_ε^m and g_σ^m.
3. Set
$$d_\varepsilon^m := \begin{cases} -g_\varepsilon^0 & \text{if } m = 0, \\ -g_\varepsilon^m + \beta_\varepsilon^m d_\varepsilon^{m-1} & \text{if } m > 0, \end{cases}$$
$$d_\sigma^m := \begin{cases} -g_\sigma^0 & \text{if } m = 0, \\ -g_\sigma^m + \beta_\sigma^m d_\sigma^{m-1} & \text{if } m > 0, \end{cases}$$
where $\beta_\varepsilon^m := \frac{\|g_\varepsilon^m\|_\Omega^2}{\|g_\varepsilon^{m-1}\|_\Omega^2}$ and $\beta_\sigma^m := \frac{\|g_\sigma^m\|_\Omega^2}{\|g_\sigma^{m-1}\|_\Omega^2}$.
4. Compute optimal step sizes as:
$$\alpha_\varepsilon^m = - \frac{\int_\Omega d_\varepsilon^m g_\varepsilon^m \mathrm{d}x}{\gamma_\varepsilon^m \int_\Omega (d_\varepsilon^m)^2 \mathrm{d}x},$$
$$\alpha_\sigma^m = - \frac{\int_\Omega d_\sigma^m g_\sigma^m \mathrm{d}x}{\gamma_\sigma^m \int_\Omega (d_\sigma^m)^2 \mathrm{d}x}.$$
5. Update the dielectric permittivity and conductivity as:
$$\varepsilon^{m+1} := \varepsilon^m + \alpha_\varepsilon^m d_\varepsilon^m, \quad \sigma^{m+1} := \sigma^m + \alpha_\sigma^m d_\sigma^m.$$
6. Compute new regularization parameters for any $p \in (0, 1)$ via iterative rules of [2] as
$$\gamma_\varepsilon^{m+1} = \frac{\gamma_\varepsilon^0}{(m+1)^p}, \qquad \gamma_\sigma^{m+1} = \frac{\gamma_\sigma^0}{(m+1)^p}$$
7. Terminate the algorithm if either $\|\varepsilon^{m+1} - \varepsilon^m\| < \eta_\varepsilon^1$ and $\|\sigma^{m+1} - \sigma^m\| < \eta_\sigma^1$, or $\|g_\varepsilon^m\| < \eta_\varepsilon^2$ or $\|g_\sigma^m\| < \eta_\sigma^2$, where η_ε^1, η_ε^2, η_σ^1 and η_σ^2 are tolerances chosen by the user. Otherwise, set $m := m + 1$ and repeat the algorithm from step 2.

The ACGA employs the following stopping criteria. The algorithm is terminated if either:

1) $\left\| \varepsilon_{h,i}^{M_i} - \varepsilon_{h,i-1}^{M_{i-1}} \right\| < \theta_\varepsilon^1$ and $\left\| \sigma_{h,i}^{M_i} - \sigma_{h,i-1}^{M_{i-1}} \right\| < \theta_\sigma^1$, or
2) $\left\| g_\varepsilon^{M_i} \right\| < \theta_\varepsilon^2$, or
3) $\left\| g_\sigma^{M_i} \right\| < \theta_\sigma^2$,

where θ_ε^1, θ_ε^2, θ_σ^1 and θ_σ^2 are tolerances chosen by the user.

Criterion 1) indicate that the ACGA is terminated once the reconstructed values of $\varepsilon_{h,i}^{M_i}$ and $\sigma_{h,i}^{M_i}$ have stabilized. Note that we always verify that the reconstructed coefficients belong to the sets of admissible parameters C_ε and C_σ defined in (28), see also (3). Criteria 2) and 3) indicate that the ACGA is terminated when the computed gradients with respect to ε or σ, respectively, become sufficiently small.

Algorithm 2: Adaptive Conjugate Gradient Algorithm (ACGA): For mesh refinements $i = 0, \ldots, G$ perform the steps below.

1. Choose initial spatial mesh $\mathbb{K}_{h,0}$ in Ω_{FEM} and set $i = 0$.
2. Compute $\varepsilon_{h,i}^{M_i}$, $\sigma_{h,i}^{M_i}$ on mesh $\mathbb{K}_{h,i}$ according to the CGA.
3. Refine all mesh elements $K_\ell \in \mathbb{K}_{h,i}$, satisfying
$$|h\varepsilon_{h,i}^{M_i}| \geq \rho_{\varepsilon_i} \max_{K_{\tilde{\ell}} \in \mathbb{K}_{h,i}} |h\varepsilon_{h,i}^{M_i}|,$$
and
$$|h\sigma_{h,i}^{M_i}| \geq \rho_{\sigma_i} \max_{K_{\tilde{\ell}} \in \mathbb{K}_{h,i}} |h\sigma_{h,i}^{M_i}|.$$
Here, $\rho_{\varepsilon_i} \in (0,1)$, $\rho_{\sigma_i} \in (0,1)$ are constants chosen by the user.
4. Construct the new mesh $\mathbb{K}_{h,i+1}$ and interpolate $\varepsilon_{h,i}^{M_i}$, $\sigma_{h,i}^{M_i}$ and the measurements E_{obs} onto it.
5. If $i > 0$, terminate the algorithm if either $\left\|\varepsilon_{h,i}^{M_i} - \varepsilon_{h,i-1}^{M_{i-1}}\right\| < \theta_\varepsilon^1$ and $\left\|\sigma_{h,i}^{M_i} - \sigma_{h,i-1}^{M_{i-1}}\right\| < \theta_\sigma^1$, or $\left\|g_\varepsilon^{M_i}\right\| < \theta_\varepsilon^2$ or $\left\|g_\sigma^{M_i}\right\| < \theta_\sigma^2$, where θ_ε^1, θ_ε^2, θ_σ^1 and θ_σ^2 are tolerances chosen by the user. Otherwise, set $i := i + 1$ and repeat the algorithm from step 2.

IV. Data preprocessing

When working with experimental data, one typically encounters a mismatch between experimental and simulated results. This discrepancy can arise from several factors, including instability in the amplitude of the emitted signals (plane waves in the case of our simulations), unwanted scattering from healthy skin, and differences between the simulated and experimental incident waves. Similar conclusions have been reported in experimental studies [34], [35], in which a numerical method for imaging buried objects using experimental backscattered time-dependent data was developed. In the current work, we apply the data preprocessing procedure developed in [34], [35] for imaging buried objects in sand, to the reconstruction of the dielectric properties of MM in the skin.

First, we note that when the incident wave E^i (plane wave in our case) interacts with a non-homogeneous domain, it generates a scattered wave, and the total field satisfies
$$E^{\mathrm{t}} = E^s + E^i.$$
According to [16], [17], the scattered field is defined as $E^s = E^{\mathrm{t}} - E^i$. For the model problem (6), E^{t} denotes the solution of the forward problem with $E = E^{\mathrm{t}}$ and with the dielectric parameters ε and σ prescribed in the investigated domain. The incident field E^i corresponds to the background medium with dielectric parameters ε_{b} and σ_{b}. In the extraction of backscattered signals for MM, the background medium is the skin without the tumor. Such a reference signal can be measured for each patient at any location on healthy skin. It is only necessary to ensure that the geometry of the healthy skin region matches that of the region containing the MM. We note that approximate depths of healthy skin and MM can be taken from [13], and these values are used in our experiments.

We now describe a procedure for isolating the backscattered electromagnetic waves generated by MM in a non-homogeneous medium. To isolate the scattered electromagnetic waves originating from MM tissue, we repeat the generation of backscattered electromagnetic fields for tissue *without* MM. That is, we repeat the simulation in the domain Ω_{FEM}, consisting of the epidermis, dermis, and fat. We then subtract the backscattered data obtained from healthy tissue, which we denote as $E^i(x,t)$, from the data produced by the total field in the presence of MM, which we denote as $E^{\mathrm{t}}(x,t)$. The resulting scattered data $E^s(x,t)$ should be dominated by the reflections caused by MM tissue, since the reflections caused by other tissue types are subtracted away. Thus, to determine the scattered data $E^s(x,t)$ from MM we compute
$$E^s(x,t) = E^{\mathrm{t}}(x,t) - E^i(x,t). \tag{25}$$
Fig. 10 shows the backscattered data produced by healthy skin with dielectric properties shown in Fig. 9. Fig. 11 shows the backscattered data produced by skin containing MM. Dielectric properties for this case are presented in Fig. 8. We note that Fig. 10 and Fig. 11 present the backscattered data for all components of the electric field. The dominant reflections arise from the second component because, in our numerical experiments, the plane wave is initialized only in this component of the electric field – see (30). This observation is theoretically justified in [32] and numerically presented in [5], [24], and in the current work.

In Fig. 12, the preprocessed data computed using (25) are shown, where we see clear reflections caused by MM tissue. Note that the MM tissue is modeled to be a hemisphere with center in the center of $\partial_1\Omega$, while other tissue types are modeled as flat layers. Therefore, a high variation in the backscattered data at the center of the observation region is expected to originate from the MM tissue.

A. Data calibration and embedding

Comparing Fig. 3 and Fig. 12, we observe that our simulated data for MM in a homogeneous domain (shown in Fig. 3) and data for MM after the preprocessing procedure (presented in Fig. 12) have different amplitudes.

Fig. 10 and Fig. 11 also show that the amplitude of the backscattered data for skin with MM and for healthy skin is nearly identical, and that the corresponding datasets are very similar. The preprocessed data shown in Fig. 12 have a much smaller amplitude than the data presented in Fig. 10 and Fig. 11. This can be explained by the fact that the dielectric properties of MM are very close to those of the epidermis and dermis (see Table 1). Consequently, the procedure (25) with these dielectric properties leads to smaller reflection amplitudes from the MM. As a result, the data for MM after the preprocessing procedure using (25) produce a scattered field $E^s(x,t)$ of small amplitude because the amplitudes of $E^{\mathrm{t}}(x,t)$ and $E^i(x,t)$ are approximately equal – see Fig. 10 and Fig. 11. From these figures, we also observe that it is visually impossible to distinguish between $E^{\mathrm{t}}(x,t)$ and $E^i(x,t)$. Only the computation of the scattered field $E^s(x,t)$ using (25) makes it possible to identify the field scattered by the MM, as shown in Fig. 12.

Thus, we define quantities, which we call calibration factors to scale preprocessed data to the same scale as that used in our ACGA simulations for MM in a homogeneous domain. In other words, we consider MM in a homogeneous domain as a calibration object with known dielectric properties. The same calibration object should be consistently used in all computational tests involving the reconstruction of MM from preprocessed data.

We note that all versions of calibration procedures are heuristic, and each yields successful ACGA reconstructions, although with different reconstruction errors. A similar conclusion regarding the calibration procedure, as well as the main idea behind the calibration procedure, has been reported in experimental studies [34], [35].

Let $E^h(x,t)$ denote the scattered data for the homogeneous domain and $E^s(x,t)$ the preprocessed scattered data where $E^s(x,t)$ is computed as in (25). Let

$$d^h(t) = \max_{\partial_1\Omega} E^h(x,t),$$
$$d^s(t) = \max_{\partial_1\Omega} E^s(x,t).$$

Version 1

The quantities $d^{\mathrm{cal}}(t) = d^s(t)/d^h(t)$ can be used as calibration factors at every time step. This means that the preprocessed data are multiplied by these calibration factors at every time step. The next step is data embedding. We embed the calibrated scattered data into the data from the homogeneous domain. To summarize data calibration and embedding steps, we finally compute the following data

$$E^{\mathrm{comp}}(x,t) = E^s(x,t)\cdot d^{\mathrm{cal}}(t) + E^h(x,t)$$

which can now be used for computations in the ACGA.

Version 2

The quantities $d^{\mathrm{cal}}(t) = d^h(t) - d^s(t)$ can also be used as calibration factors at every time step. The data calibration and embedding procedure is then defined as follows:

$$E^{\mathrm{comp}}(x,t) = E^s(x,t) + d^{\mathrm{cal}}(t) + E^h(x,t) \tag{26}$$

which can also be used for computations in the ACGA.

Version 3

The data calibration without an embedding procedure with $d^{\mathrm{cal}}(t) = d^h(t) - d^s(t)$ can be defined as follows:

$$E^{\mathrm{comp}}(x,t) = E^s(x,t) + d^{\mathrm{cal}}(t) \tag{27}$$

which can also be employed in computations using the ACGA.

The second version of data calibration yields better reconstruction results for both parameters ε_w and σ_w which we report in the next subsections. Fig. 14 shows the calibrated and embedded data obtained using the second version of the calibration procedure.

V. Numerical examples

In this section, we present numerical examples that illustrate the theoretical results and demonstrate the performance of the ACGA. All the numerical computations were performed in `C++` with the `PETSc` library [39] and `WavES` package [40]. All the visualizations are generated using `ParaView` [41] and `GiD` [42].

We show several numerical tests. First, we apply the ACGA (Algorithm 2) in a setting with only two tissue types, MM and non-melanoma, corresponding to a homogeneous media. Then we present results in a non-homogeneous setting, for MM placed in skin. Specifically, we apply the data preprocessing procedure described in Section IV to isolate the reflected electromagnetic waves caused by MM when several tissue types other than MM are present, such as epidermis, dermis, and fat, simulating a more realistic scenario. Using the extracted backscattered data, we reconstruct weighted ε_w and σ_w, illustrating the dependence on initial guesses ε^0 and σ^0. We also showcase how calibrating the observed data and smoothing reconstructed results reduce the dependence on the initial guess.

The computational domain has been designed to reflect a realistic physical setting, following the approach developed in [4], [24], where MM in the skin is modeled as a hemisphere – see Fig. 8.

We restrict our attention to a frequency of 6 GHz and use the known values of permittivity and conductivity for this frequency for different tissue types from [8]. The initial regularization parameters are set to $\gamma_\varepsilon^0 = \gamma_\sigma^0 = 0.01$. Our domain of interest is $\Omega := (-2,12)\times(-2,12)\times(-2,12)$ and the computational finite element domain is $\Omega_{\mathrm{FEM}} := (0,10)\times(0,10)\times(0,10)$. Finally, we set the finite difference domain as $\Omega_{\mathrm{FDM}} = \Omega \setminus ((1,9)\times(1,9)\times(1,9))$. All spatial dimensions are given in millimeters.

In all experiments we assume $\varepsilon \in C_\varepsilon$ and $\sigma \in C_\sigma$ where we set $\bar{\varepsilon} = 10$ and $\bar{\sigma} = 2$. More precisely, we assume that the coefficients satisfy $\varepsilon_w \in C_\varepsilon$ and $\sigma_w \in C_\sigma$, where

$$\begin{aligned} C_\varepsilon &:= \{\varepsilon \in C^2(\overline{\Omega}) : \varepsilon(x) = 1 \ \forall x \in \Omega_{\mathrm{FDM}}, \\ &\qquad \varepsilon(x) \in [1,10] \ \forall x \in \Omega_{\mathrm{FEM}}\} \\ C_\sigma &:= \{\sigma \in C^2(\overline{\Omega}) : \sigma(x) = 0 \ \forall x \in \Omega_{\mathrm{FDM}}, \\ &\qquad \sigma(x) \in [0,2.0] \ \forall x \in \Omega_{\mathrm{FEM}}\} \end{aligned} \tag{28}$$

To reduce computational time of the overall reconstruction procedure, we chose the maximum number of iterations as $M = 5$ for the CGA on the coarse mesh $K_{h,0}$, and $M = 1$ on all subsequently refined meshes $K_{h,i}$, where i denotes the number of mesh refinements. This explains why the ACGA converges in the first iteration on the refined meshes. We note that we obtain $\|\varepsilon_w\|_\infty = 10$ on all meshes because the step size in the CGA was selected to reach this value consistently, thereby reducing computational time.

We set the final time to $T = 12$. The motivation behind this choice is presented later. The boundary Γ is divided into subsets $\Gamma = \partial_1\Omega \cup \partial_2\Omega \cup \partial_3\Omega$, where

$$\begin{aligned}
\partial_1\Omega &= \{(x_1, x_2) \in \Omega : x_3 = 12\},\\
\partial_2\Omega &= \{(x_1, x_2) \in \Omega : x_3 = -2\},\\
\partial_3\Omega &= \Gamma \setminus (\partial_1\Omega \cup \partial_2\Omega)\,.
\end{aligned}$$

We also define the time-dependent boundaries, $\Gamma_{1,1} = \partial_1\Omega \times (0, t_1]$ and $\Gamma_{1,2} = \partial_1\Omega \times (t_1, T)$ for some $t_1 \in (0, T)$ as well as $\Gamma_2 = \partial_2\Omega \times (0, T)$ and $\Gamma_3 = \partial_3\Omega \times (0, T)$. Setting $f_0(x) = f_1(x) = 0$ for all $x \in \Omega$, the stabilized forward problem then becomes: Find E such that

$$\begin{aligned}
\varepsilon\frac{\partial^2 E}{\partial t^2} + \sigma\frac{\partial E}{\partial t} - \Delta E \quad & \\
-\nabla\nabla\cdot((\varepsilon - 1)\,E) = 0, \quad & \text{in } \Omega_T, && (29a)\\
E(x,0) = \frac{\partial E}{\partial t}(x,0) = 0, \quad & \text{in } \Omega, && (29b)\\
\frac{\partial E}{\partial \mathbf{n}} = Q(t), \quad & \text{on } \Gamma_{1,1}, && (29c)\\
\frac{\partial E}{\partial \mathbf{n}} + \frac{\partial E}{\partial t} = 0, \quad & \text{on } \Gamma_{1,2}\cup\Gamma_2, && (29d)\\
\frac{\partial E}{\partial \mathbf{n}} = 0, \quad & \text{on } \Gamma_3. && (29e)
\end{aligned}$$

Here, $Q(t) = (Q_1, Q_2, Q_3)(t) = (0, Q_2, 0)(t)$ is a plane wave, with

$$Q_2(t) = \begin{cases} \sin(\omega t) & \text{if } t \in (0, \frac{2\pi}{\omega}),\\ 0 & \text{if } t \geq \frac{2\pi}{\omega}, \end{cases} \qquad (30)$$

initialized only for the second component of the electric field. The function $Q(t)$ produces a plane wave that passes through the domain. We consider time-dependent observations only on $\partial_1\Omega$ and therefore consider only the backscattered data of the electric field.

We introduce a uniform mesh Ω_{FDM_h} on Ω_{FDM} consisting of hexahedra, see Fig. 1 in [24]. On Ω_{FEM}, a mesh K_h of tetrahedral elements is introduced. These meshes are created such that all points $x_h \in \Omega_{\mathrm{FDM}_h} \cap \Omega_{\mathrm{FEM}}$ are also in K_h. The time interval is discretized into $N = 500$ partitions, such that the time step $\tau = T/N = 0.024$ satisfies the CFL stability condition derived in [7] ensuring stable solutions from the explicit methods.

To minimize memory usage while still satisfying the CFL condition, great care was taken in choosing the final time T. We choose $T = 12$ so that the plane wave $Q(t)$ can pass through the whole domain Ω, to produce the best possible reflections from MM using $\omega = 40$ in (30).

The values of the different tissue types at 6 GHz are summarized in Table 1 and are based on data from [13], [38], [8], and [24]. The table presents real-world measurements alongside the weighted model parameter values used in the numerical examples.

TABLE 1: Realistic values of ε and σ (S/m) at 6 GHz for skin with MM as well as weighted values ε_w and σ_w used for testing. Here, the depth of MM is in mm and is measured from the surface of the skin. The depth of the MM is taken from [13].

Values	Real		Test 1 & 2		Test 3,4 & 5		
Tissue type	ε	σ (S/m)	ε_w	σ_w (S/m)	ε_w	σ_w (S/m)	Depth (mm)
Im. medium	32	4	1	0	6.4	0.08	-2
Epidermis	35	4	1	0	7	0.08	1
Dermis	40	9	1	0	8	0.18	3.5
Fat	9	1	1	0	1.8	0.02	5.5
Tum. stage 1	45	6	8	1.2	9	0.12	< 1
Tum. stage 2	50	6	9	1.2	9	0.12	> 1

A. Computational setup at 6 GHz

Table 1 lists the specific values taken in all our numerical tests. These values are used only to generate the observed electric field E_{obs}, much as in real-world applications. The main difference is that, in the present work, the observed electric field is simulated.

In order to generate the electric field E_{obs} in the observation points $\{x_{\mathrm{obs},i}\}_{i=1}^{M_{\mathrm{obs}}}$, we assign values to the functions ε_w and σ_w according to Table 1 such that conditions (3) are satisfied. Using these values of ε_w and σ_w, the forward problem (29) is solved using the ACGA on a mesh that has been adaptively refined five times. This mesh is refined only in the mesh elements $K_\ell \in \mathbb{K}_h$ that contain MM. Note that this refined mesh is not the same as the one generated later by the ACGA when recreating ε_w and σ_w. Since real-life measurements are invariably affected by noise, we add synthetic noise to the solution at the desired observation points. The computed solution E at the observation points $\{x_{\mathrm{obs},i}\}_{i=1}^{M_{\mathrm{obs}}} \subset \Omega_{\mathrm{FDM}_h} \cup K_h$ is stored as

$$E_{\mathrm{obs}}(x_{\mathrm{obs},i}, t_k) = (1 + \xi\epsilon_{i,t_k})E(x_{\mathrm{obs},i}, t_k) \qquad (31)$$

for all $i \in \{0, \ldots, M_{\mathrm{obs}}\}$, where $t_k = k\tau$ for all $k \in \{0, \ldots, N\}$. Here, $\xi \in (0, 1)$ is the noise level and ϵ_{i,t_k} are random numbers generated on the interval $[-1, 1]$ for each time $t_k = k\tau$, where $k \in \{0, \ldots, N\}$. For all computations, the noise level is set to $\xi = 0.1$, which corresponds to 10% noise in the data. In all computations, the noisy data are smoothed by using $\epsilon_{i,t_k} = 1$ in (31).

We choose the initial guesses $\varepsilon_w^0 = 1$ and $\sigma_w^0 = 0$ on the meshes Ω_{FDM_h} and $\mathbb{K}_{h,0} = \mathbb{K}_h$. We then set $\overline{\varepsilon} = 10$ and $\overline{\sigma} = 2$ in (3) thereby constraining the reconstructed values of ε_w and σ_w to remain below 10 and 2, respectively. The mesh refinement indicators in the ACGA were chosen as follows:

$$\rho_{\varepsilon_i} = \begin{cases} 0.4 & \text{if } i < 5,\\ 0.5 & \text{else,} \end{cases} \qquad (32)$$

and

$$\rho_{\sigma_i} = \begin{cases} 0.4 & \text{if } i < 5,\\ 0.5 & \text{else.} \end{cases} \qquad (33)$$

In order to reduce computational time, we choose a maximum number of iterations of $M = 5$ for the CGA (Algorithm 1), together with a maximum of $G = 8$ iterations for the ACGA (Algorithm 2). We also use constant step sizes as

$$\alpha_\varepsilon^m = \begin{cases} 100 & \text{if } \|\varepsilon_w^m\|_\infty < 9, \\ 0.01 & \text{else,} \end{cases}$$

and

$$\alpha_\sigma^m = \begin{cases} -10 & \text{if } |\min \sigma_w^m| < 0.5, \\ -0.01 & \text{else.} \end{cases}$$

In our numerical experiments, we use heuristic step sizes derived numerically by running the ACGA several times on the same data. These step sizes have provided accurate reconstructions of dielectric property values in our numerical settings while reducing the overall computational time of the reconstruction algorithm. Computing optimal step sizes requires additional computational time for the overall reconstruction procedure. We plan to investigate this in future research, including a comparison of computational time between constant and optimal step sizes.

During the numerical experiments in Test 1, we observed that the ACGA satisfied the convergence criterion, but the correct depth of the MM was not reconstructed (see Fig. 4). Therefore, in subsequent tests, we applied a smoothing procedure as follows. At each step of the CGA, the computed finite element solution is smoothed according to the following rule. If the element under consideration is not a boundary element, its nodal values are replaced by the average nodal value of the element and its neighboring elements. If the element is a boundary element, its nodal values are set to the average of the nodal values within that element only, without considering neighboring elements. This procedure helps remove artifacts and enabled a more accurate reconstruction of the MM depth, as demonstrated by the reconstructions obtained in Tests 2, 4, and 5.

B. MM in a homogeneous domain

We begin our numerical tests by considering MM in a homogeneous domain. Fig. 2 provides an overview of the exact distributions of ε_w and σ_w, while Table 1 lists the corresponding parameter values. In both Tests 1 and 2, we reconstruct MM located in a homogeneous domain.

Test 1

In this section, we consider only two tissue types: MM and non-melanoma tissue. In Fig. 3, we show the simulated observations E_{obs} at the observation points after smoothing the noisy data.

Here, we use the initial values of $\varepsilon_w^0 = 1$ and $\sigma_w^0 = 0$. Fig. 4 shows the reconstructed $\varepsilon_{w,h}$ and $\sigma_{w,h}$ alongside the exact solutions. Here, $\|\varepsilon_{w,h}\|_\infty = 10$ and $\|\sigma_{w,h}\|_\infty \approx 1.29$, see Table 2 for the ACGA convergence results. The table also presents the number of nodes in the generated adaptively refined finite element meshes which are shown in Fig. 5. It can be observed from both the figure and the table that mesh refinement first occurs during the third refinement iteration of the ACGA.

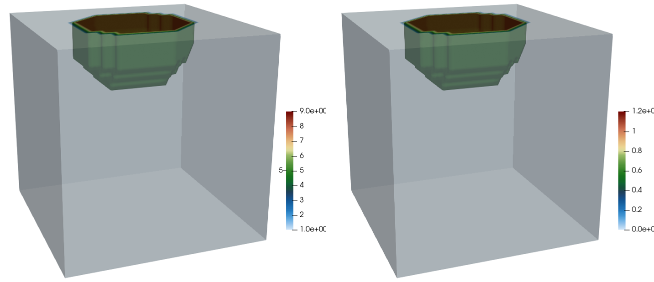

(a) ε_w (b) σ_w

FIGURE 2: Spatial distribution of ε_w and σ_w in the homogeneous domain Ω_{FEM}, with $\|\varepsilon_w(x)\|_\infty = 9$ and $\sigma_w(x) = 1.2$ for x inside MM and $\varepsilon_w(x) = 1$ and $\sigma_w(x) = 0$ for x outside MM.

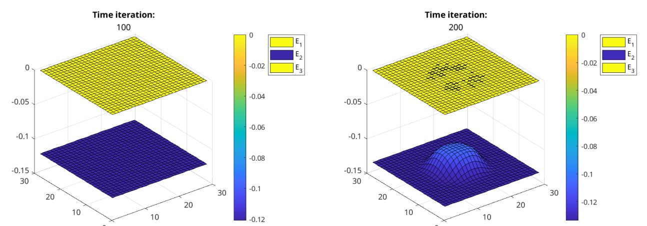

(a) $t = 2.4$ (b) $t = 4.8$

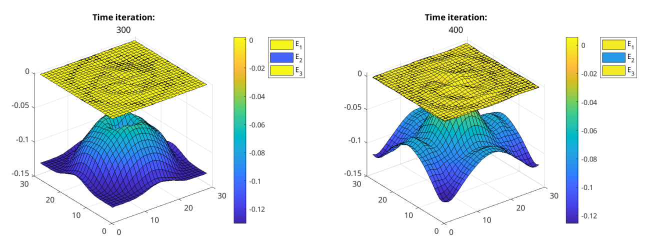

(c) $t = 7.2$ (d) $t = 9.6$

FIGURE 3: Test 1. Simulated noisy backscattered data $E = E_{\text{obs}}$ after smoothing for different times $t \in (0, T)$ in a homogeneous domain with MM. The noise level in the data for the electric field is $\xi = 0.1$.

Test 2

Here, we use the same setup as in Test 1, except that the smoothing procedure described above, is applied to the reconstructed functions. The convergence results of the ACGA are presented in Table 3, with illustrations of the reconstructed $\varepsilon_{w,h}$ and $\sigma_{w,h}$ shown in Fig. 6. The projections of the adaptively refined finite element mesh obtained after the final refinement are shown in Fig. 7.

This article has been accepted for publication in IEEE Open Journal of Antennas and Propagation. This is the author's version which has not been fully edited and content may change prior to final publication. Citation information: DOI 10.1109/OJAP.2026.3714060

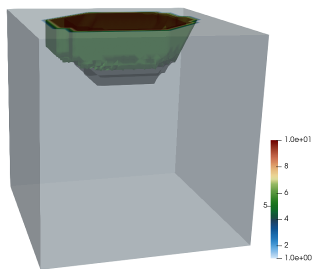

(a) $\varepsilon_{w,h}$

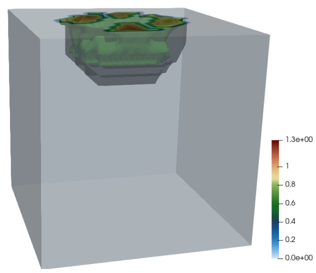

(b) $\sigma_{w,h}$

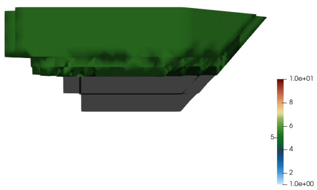

(c) $\varepsilon_{w,h}$. Side view.

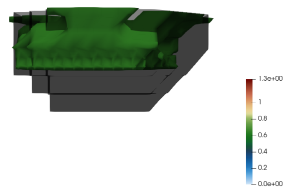

(d) $\sigma_{w,h}$. Side view.

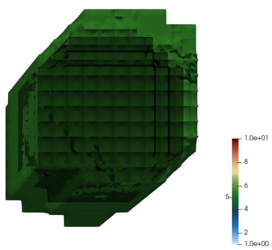

(e) $\varepsilon_{w,h}$. Top view.

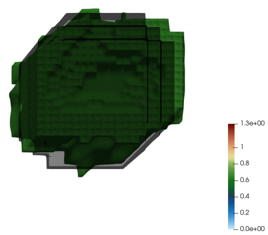

(f) $\sigma_{w,h}$. Top view.

FIGURE 4: Test 1. Solid isosurfaces representing MM in the reconstructed solutions $\varepsilon_{w,h}$ and $\sigma_{w,h}$, together with opaque isosurfaces corresponding to the exact reference solutions ε_w and σ_w. Reconstructions are obtained on $\mathbb{K}_{h,7}$.

TABLE 2: Test 1. Computational results of the reconstructions $\|\varepsilon_{w,h}\|_\infty$ and $\|\sigma_{w,h}\|_\infty$, respectively, at 6 GHz. The results relate to the homogeneous domain with initial values of $\varepsilon_w^0 = 1$ and $\sigma_w^0 = 0$. Here, i denotes the iteration of the ACGA, M_i is the number of iterations of the CGA, R_i is the total number of points in mesh $\mathbb{K}_{h,i}$.

i	M_i	R_i	$\|\varepsilon_{w,h}\|_\infty$	$\|\sigma_{w,h}\|_\infty$	$\|g_\varepsilon\|/R_i$	$\|g_\sigma\|/R_i$
0	2	9261	10	0.73	$9.3173 \cdot 10^{-6}$	$6.1434 \cdot 10^{-6}$
1	1	9261	10	0.71	$9.3173 \cdot 10^{-6}$	$6.1434 \cdot 10^{-6}$
2	1	9261	10	0.82	$9.9274 \cdot 10^{-6}$	$4.9566 \cdot 10^{-5}$
3	1	9385	10	0.91	$1.1243 \cdot 10^{-5}$	$3.4783 \cdot 10^{-6}$
4	1	9857	10	1.00	$1.0696 \cdot 10^{-5}$	$3.3198 \cdot 10^{-6}$
5	1	11332	10	1.10	$9.3224 \cdot 10^{-6}$	$2.9490 \cdot 10^{-6}$
6	1	13325	10	1.19	$7.8202 \cdot 10^{-6}$	$2.5610 \cdot 10^{-6}$
7	1	19255	10	1.29	$5.4447 \cdot 10^{-6}$	$1.7890 \cdot 10^{-6}$

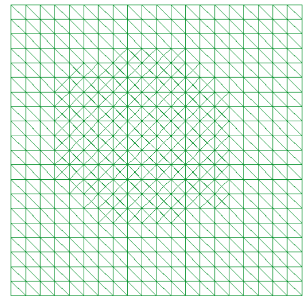

(a) $i = 4$. Top view.

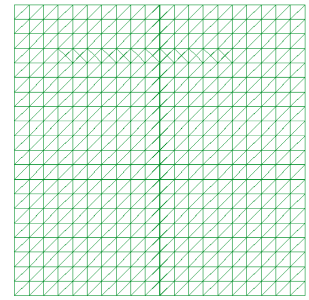

(b) $i = 4$. Side view.

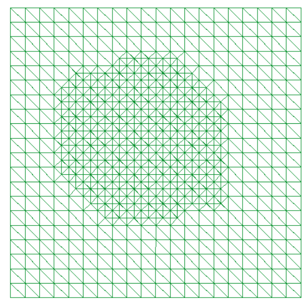

(c) $i = 5$. Top view.

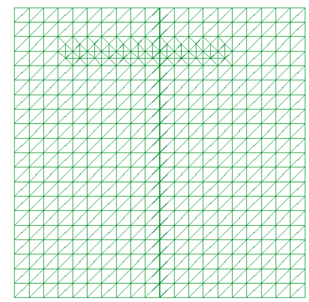

(d) $i = 5$. Side view.

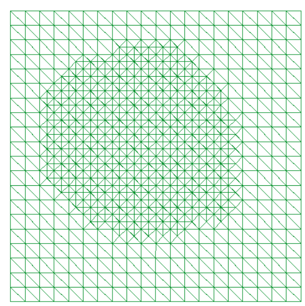

(e) $i = 6$. Top view.

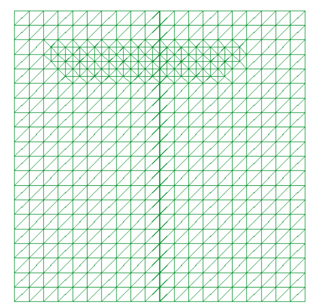

(f) $i = 6$. Side view.

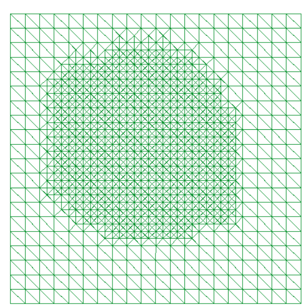

(g) $i = 7$. Top view.

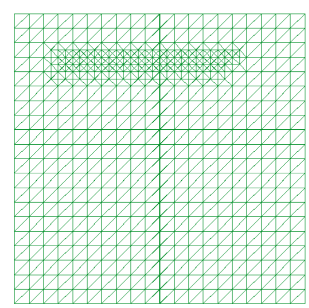

(h) $i = 7$. Side view.

FIGURE 5: Test 1. Adaptively refined finite element meshes $\mathbb{K}_{h,i}$ for $i \in \{4, 5, 6, 7\}$ generated using the ACGA with the mesh refinement parameters given in (32) and (33).

This article has been accepted for publication in IEEE Open Journal of Antennas and Propagation. This is the author's version which has not been fully edited and content may change prior to final publication. Citation information: DOI 10.1109/OJAP.2026.3714060

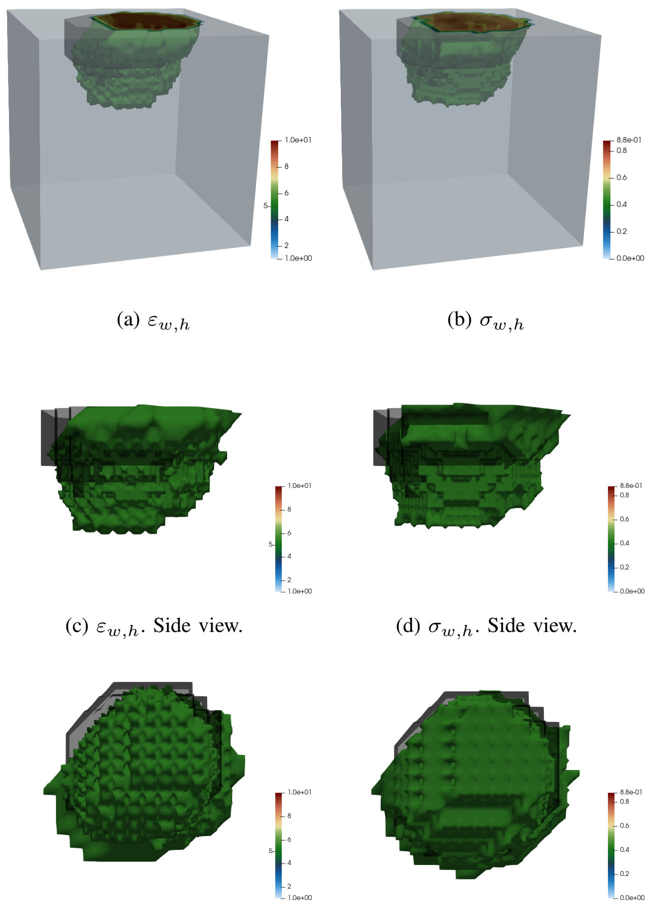

(a) $\varepsilon_{w,h}$ (b) $\sigma_{w,h}$

(c) $\varepsilon_{w,h}$. Side view. (d) $\sigma_{w,h}$. Side view.

(e) $\varepsilon_{w,h}$. Top view. (f) $\sigma_{w,h}$. Top view.

FIGURE 6: Test 2. Generated isosurfaces of the reconstructed $\varepsilon_{w,h}$ and $\sigma_{w,h}$ on $\mathbb{K}_{h,4}$ in the homogeneous domain. Initial values were chosen as $\varepsilon_w^0 = 1$ and $\sigma_w^0 = 0$. The isosurfaces of the reference solution are shown in opaque dark gray.

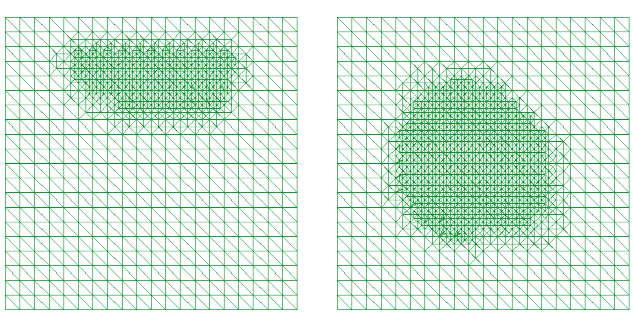

(a) Side view (b) Top view

FIGURE 7: Test 2. Projections of the adaptively refined finite element mesh $\mathbb{K}_{h,4}$ after 4 mesh refinements.

TABLE 3: Test 2. Computational results of the reconstructions $\|\varepsilon_{w,h}\|_\infty$ and $\|\sigma_{w,h}\|_\infty$ at 6 GHz. The results relate to the homogeneous domain with initial values of $\varepsilon_w^0 = 1$ and $\sigma_w^0 = 0$, with smoothing applied at each iteration. Here, i denotes the iteration of the ACGA, M_i is the number of iterations of the CGA, R_i is the total number of points in mesh $\mathbb{K}_{h,i}$.

i	M_i	R_i	$\|\varepsilon_{w,h}\|_\infty$	$\|\sigma_{w,h}\|_\infty$	$\|g_\varepsilon\|/R_i$	$\|g_\sigma\|/R_i$
0	4	9261	10	0.9239	$7.520 \cdot 10^{-6}$	$8.672 \cdot 10^{-6}$
1	1	10024	10	0.6468	$6.947 \cdot 10^{-6}$	$8.012 \cdot 10^{-6}$
2	1	13373	10	0.7270	$4.746 \cdot 10^{-6}$	$4.422 \cdot 10^{-6}$
3	1	27606	10	0.7990	$2.380 \cdot 10^{-6}$	$2.149 \cdot 10^{-6}$
4	1	87662	10	0.8768	$7.526 \cdot 10^{-7}$	$7.071 \cdot 10^{-7}$

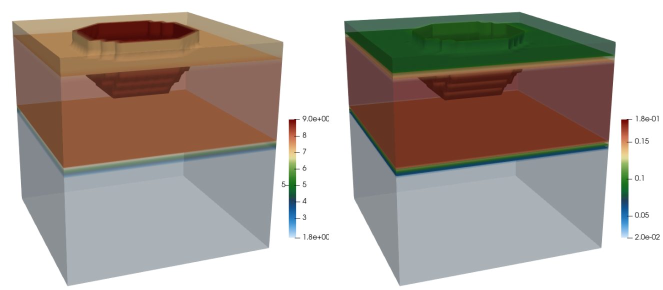

(a) ε_w (b) σ_w

FIGURE 8: Spatial distribution of ε_w and σ_w in Ω_{FEM} in the non-homogeneous computational domain. Values of $\varepsilon_w(x)$ and $\sigma_w(x)$ are chosen as in Tests 3, 4 and 5 in the Table 1.

From the reconstructions shown in Fig. 6, we conclude that the smoothing procedure enabled a more accurate reconstruction of the MM depth than that obtained in Test 1.

C. MM in skin

We now move to the non-homogeneous setting by introducing additional tissue types into the domain. In the non-homogeneous case, the domain Ω_{FEM} consists of MM, epidermis, dermis, and fat. Here, are assigned the values given in Table 1; see also Fig. 8.

Applying a procedure similar to that in the homogeneous setting, but adapted to the non-homogeneous domain, yields backscattered observations that also contain reflections caused by tissue types other than the MM. We therefore seek to isolate the backscattered data originating from the MM tissue.

Test 3

This section presents the results of applying the ACGA to MM in the skin using the extracted scattered electric field E^s originating from the MM tissue.

Test 3 is performed with the backscattered data obtained from (25), but without applying the calibration procedure to these data. We note that the ACGA is locally convergent, and

This article has been accepted for publication in IEEE Open Journal of Antennas and Propagation. This is the author's version which has not been fully edited and content may change prior to final publication. Citation information: DOI 10.1109/OJAP.2026.3714060

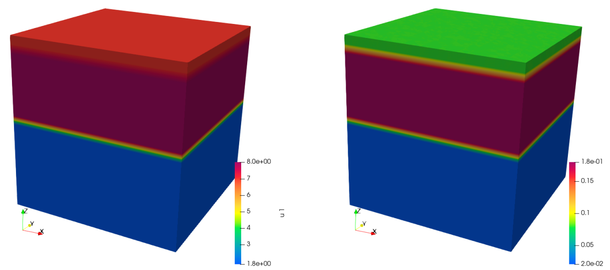

(a) ε_w (b) σ_w

FIGURE 9: Spatial distribution of ε_w and σ_w in Ω_{FEM} in the non-homogeneous computational domain consisting only of healthy skin. Values of $\varepsilon_w(x)$ and $\sigma_w(x)$ are chosen as in Tests 3, 4 and 5 in the Table 1.

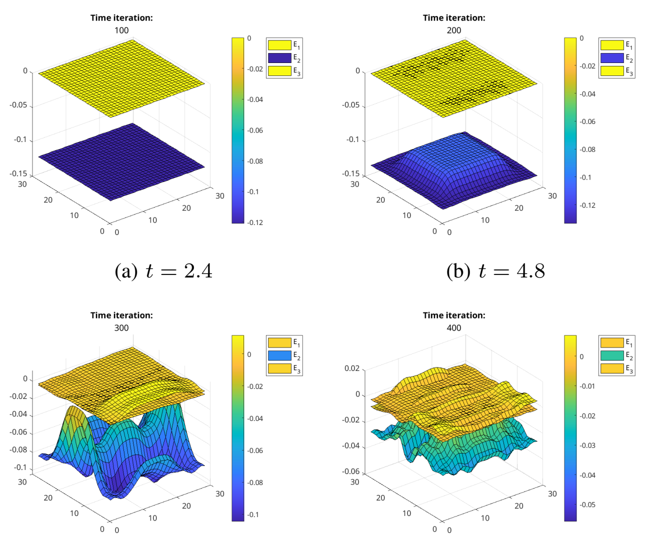

(a) $t = 2.4$ (b) $t = 4.8$

(c) $t = 7.2$ (d) $t = 9.6$

FIGURE 10: Test 3. Backscattered data computed by solving the forward problem for different times $t \in (0, T)$ for skin tissue without MM, as presented in Fig. 9. The data were generated using $\xi = 0.1$ in (31), corresponding to 10% noise in the data, after the smoothing procedure.

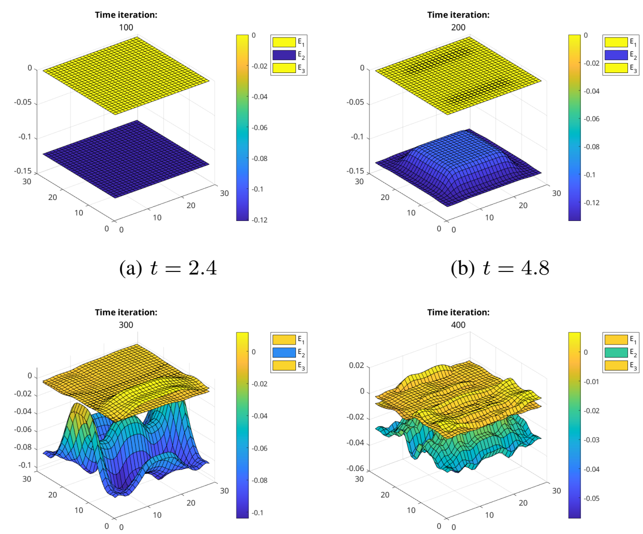

(a) $t = 2.4$ (b) $t = 4.8$

(c) $t = 7.2$ (d) $t = 9.6$

FIGURE 11: Test 3. Backscattered data computed by solving the forward problem for different times $t \in (0, T)$ for skin tissue with MM, as presented in Fig. 8. The data were generated using $\xi = 0.1$ in (31), corresponding to 10% noise in the data, after the smoothing procedure.

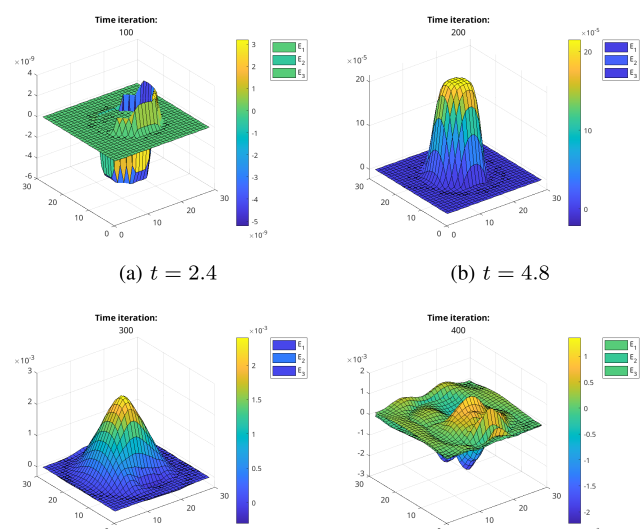

(a) $t = 2.4$ (b) $t = 4.8$

(c) $t = 7.2$ (d) $t = 9.6$

FIGURE 12: Test 3. Preprocessed backscattered data computed using (25) for different times $t \in (0, T)$ generated using $\xi = 0.1$ in (31), corresponding to 10% noise in the data, after the smoothing procedure.

its results depend on a good initial guess for the parameters ε_w^0 and σ_w^0. To illustrate this, we performed computations using two different sets of initial guesses.

Using the same setup as in Test 1 together with the initial guesses $\varepsilon_w^0 = 1$ and $\sigma_w^0 = 0$ yields a poor reconstruction, which is therefore omitted. However, when the ACGA is initialized with the solution obtained after the first ACGA iteration in Test 1, or equivalently with the initial guesses $\varepsilon_w^0 = \varepsilon_{homo}^1$ and $\sigma_w^0 = \sigma_{homo}^1$, where ε_{homo}^1 and σ_{homo}^1 denote the solutions obtained on the homogeneous domain in Test 1 using the mesh $K_{h,0}$, we obtain significantly

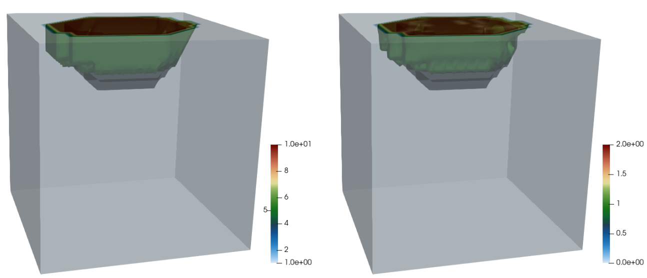

(a) $\varepsilon_{w,h}$ (b) $\sigma_{w,h}$

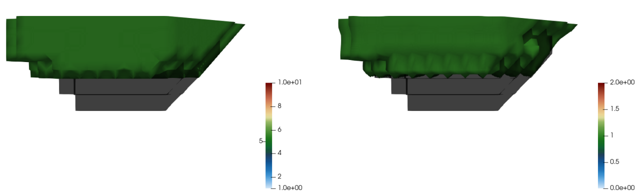

(c) $\varepsilon_{w,h}$. Side view. (d) $\sigma_{w,h}$. Side view.

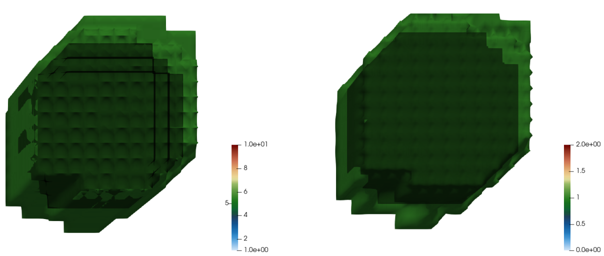

(e) $\varepsilon_{w,h}$. Top view. (f) $\sigma_{w,h}$. Top view.

FIGURE 13: Test 3. Solid isosurfaces of MM in the reconstructed solutions $\varepsilon_{w,h}$ and $\sigma_{w,h}$, together with opaque isosurfaces of the exact reference solutions ε_w and σ_w. Reconstructions are obtained on $\mathbb{K}_{h,5}$ with mesh refinement parameter defined in (32) and (33).

TABLE 4: Test 3. Computational results of the reconstructions $\|\varepsilon_{w,h}\|_\infty$ and $\|\sigma_{w,h}\|_\infty$ at 6 GHz. The results relate to the non-homogeneous domain with the initial values $\varepsilon_w^0 = \varepsilon_{homo}^1$ and $\sigma_w^0 = \sigma_{homo}^1$, where ε_{homo}^m and σ_{homo}^m denote the solutions obtained on the homogeneous domain in Test 1. Here, i is the iteration of the ACGA, M_i is the number of iterations of the CGA, R_i is the total number of points in mesh $\mathbb{K}_{h,i}$.

i	M_i	R_i	$\|\varepsilon_{w,h}\|_\infty$	$\|\sigma_{w,h}\|_\infty$	$\|g_\varepsilon\|/R_i$	$\|g_\sigma\|/R_i$
0	2	9261	10	1.34	$1.3006 \cdot 10^{-5}$	$3.0550 \cdot 10^{-5}$
1	1	9261	10	1.10	$1.3006 \cdot 10^{-5}$	$3.0550 \cdot 10^{-5}$
2	1	9261	10	1.49	$1.3673 \cdot 10^{-5}$	$2.6668 \cdot 10^{-5}$
3	1	9385	10	1.77	$1.2931 \cdot 10^{-5}$	$2.0050 \cdot 10^{-5}$
4	1	9857	10	2.00	$1.2304 \cdot 10^{-5}$	$1.9034 \cdot 10^{-5}$
5	1	11332	10	2.00	$1.0767 \cdot 10^{-5}$	$1.6786 \cdot 10^{-5}$

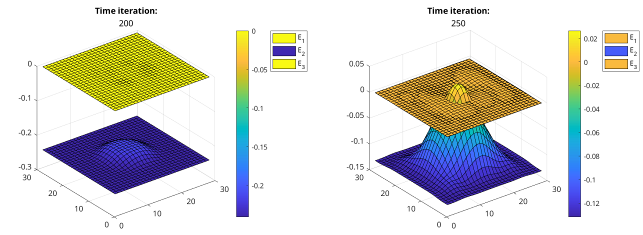

(a) $t = 4.8$ (b) $t = 6.0$

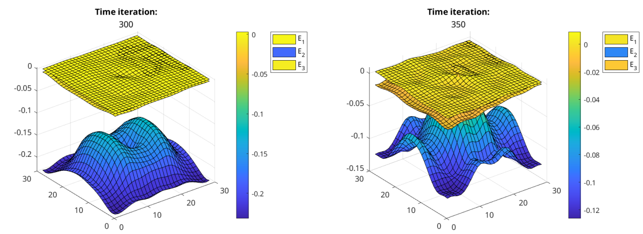

(c) $t = 7.2$ (d) $t = 8.4$

FIGURE 14: Test 4. Preprocessed, calibrated, and embedded backscattered data for different times $t \in (0, T)$ computed using (26).

improved results in terms of the geometrical shape of the reconstructed MM, as shown in Fig. 13. From the results of Test 1 presented in Table 2, we observe that the reconstructed values are $\|\varepsilon_{homo}^1\|_\infty = 10$ and $\|\sigma_{homo}^1\|_\infty = 0.73$. Hence, these reconstructed values provide good initial guesses for the second ACGA run.

Table 4 reports the maximum norms of the reconstructed $\varepsilon_{w,h}$ and $\sigma_{w,h}$. We observe that the final reconstructions $\|\varepsilon_{w,h}\|_\infty = 10$ and $\|\sigma_{w,h}\|_\infty = 2.0$ are obtained on the mesh $K_{h,5}$. These values overestimate the exact values of $\|\varepsilon_w\|_\infty$ and $\|\sigma_w\|_\infty$; see reference values for this test in Table 1. We note that the values $\|\varepsilon_{w,h}\|_\infty = 10$ and $\|\sigma_{w,h}\|_\infty = 2.0$ coincide with the upper bounds $\overline{\varepsilon}$ and $\overline{\sigma}$ of the admissible parameter sets defined in (3) and (28).

Based on the results of this test, we conclude that using only the scattered data E^s is insufficient to obtain accurate quantitative and qualitative reconstructions. Additional calibration and embedding procedures applied to the scattered data E^s are therefore necessary to improve the reconstruction results.

Test 4

In this setting, we again consider MM in skin, but here the preprocessed data are calibrated as described in Section A using (26). Furthermore, the FEM solutions are smoothed at each iteration, as in Test 2. The initial values used here are $\varepsilon_w^0 = 1$ and $\sigma_w^0 = 0$, as in the homogeneous setting. The results are summarized in Table 5, the reconstructed solutions $\varepsilon_{w,h}$ and $\sigma_{w,h}$ are shown in Fig. 15, and the resulting FEM mesh is shown in Fig. 16.

TABLE 5: Test 4. Computational results of the reconstructions $\|\varepsilon_{w,h}\|_\infty$ and $\|\sigma_{w,h}\|_\infty$ at 6 GHz. The results relate to the non-homogeneous domain using the initial values $\varepsilon_w^0 = 1$ and $\sigma_w^0 = 0$, with smoothing applied at each iteration. Here, i is the iteration of the ACGA, M_i is the number of iterations of the CGA, R_i is the total number of points in mesh $\mathbb{K}_{h,i}$.

i	M_i	R_i	$\|\varepsilon_{w,h}\|_\infty$	$\|\sigma_{w,h}\|_\infty$	$\|g_\varepsilon\|/R_i$	$\|g_\sigma\|/R_i$
0	3	9261	10	0.2367	$2.761 \cdot 10^{-5}$	$9.006 \cdot 10^{-6}$
1	1	10112	10	0.1375	$2.529 \cdot 10^{-5}$	$8.248 \cdot 10^{-6}$
2	1	13365	10	0.1609	$1.929 \cdot 10^{-5}$	$6.497 \cdot 10^{-6}$
3	1	26643	10	0.1831	$9.641 \cdot 10^{-6}$	$3.250 \cdot 10^{-6}$
4	1	79440	10	0.2061	$3.209 \cdot 10^{-6}$	$1.092 \cdot 10^{-6}$

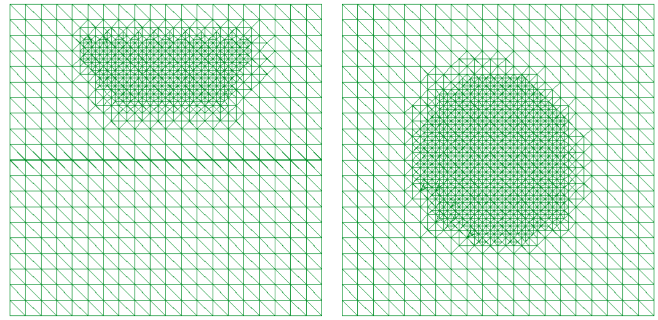

(a) Side view (b) Top view

FIGURE 16: Test 4. Projections of the adaptively refined finite element mesh $\mathbb{K}_{h,4}$ after 4 mesh refinements.

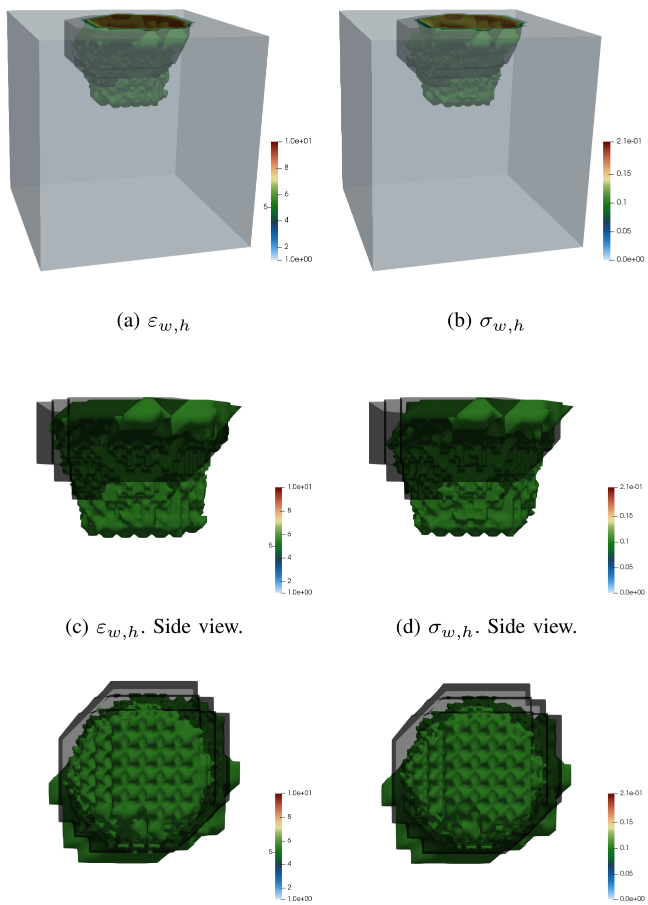

(a) $\varepsilon_{w,h}$ (b) $\sigma_{w,h}$

(c) $\varepsilon_{w,h}$. Side view. (d) $\sigma_{w,h}$. Side view.

(e) $\varepsilon_{w,h}$. Top view. (f) $\sigma_{w,h}$. Top view.

FIGURE 15: Test 4. Reconstructed isosurfaces of $\varepsilon_{w,h}$ and $\sigma_{w,h}$ on $\mathbb{K}_{h,4}$ in non-homogeneous medium using preprocessed and calibrated data, with initial values $\varepsilon_w^0 = 1$ and $\sigma_w^0 = 0$. The isosurfaces of the reference solutions are displayed in opaque dark gray.

TABLE 6: Test 5. Computational results of the reconstructions $\|\varepsilon_{w,h}\|_\infty$ and $\|\sigma_{w,h}\|_\infty$ at 6 GHz. The results relate to the non-homogeneous domain with the initial values $\varepsilon_w^0 = 1$ and $\sigma_w^0 = 0$, while applying smoothing at each iteration. Here, i is the iteration of the ACGA, M_i is the number of iterations of the CGA, R_i is the total number of points in mesh $\mathbb{K}_{h,i}$.

i	M_i	R_i	$\|\varepsilon_{w,h}\|_\infty$	$\|\sigma_{w,h}\|_\infty$	$\|g_\varepsilon\|/R_i$	$\|g_\sigma\|/R_i$
0	4	9261	10	1.150	$1.588 \cdot 10^{-5}$	$5.192 \cdot 10^{-6}$
1	1	10388	10	0.8590	$1.416 \cdot 10^{-5}$	$4.629 \cdot 10^{-6}$
2	1	13881	10	1.039	$1.302 \cdot 10^{-5}$	$8.784 \cdot 10^{-6}$
3	1	28228	10	1.296	$6.401 \cdot 10^{-6}$	$4.534 \cdot 10^{-6}$
4	1	83130	10	1.542	$2.171 \cdot 10^{-6}$	$1.606 \cdot 10^{-6}$

The ACGA converged with $\|\sigma_{w,h}\|_\infty \approx 0.21$, which somewhat overestimates the reference value of $\|\sigma_w\|_\infty = 0.12$ (see Table 1).

Test 5

In this setting, we repeat the setup from Test 4, except that the data are calibrated without the embedding procedure using (27). The results are summarized in Table 6. Visualizations of the reconstructed solutions $\varepsilon_{w,h}$ and $\sigma_{w,h}$ are shown in Fig. 17.

From the reconstructed values in Table 6, we observe that high contrast is achieved for both $\varepsilon_{w,h}$ and $\sigma_{w,h}$, with $\|\varepsilon_{w,h}\|_\infty = 10$ and $\|\sigma_{w,h}\|_\infty \approx 1.54$.

D. Discussion on reconstruction results

Table 7 summarizes the final reconstruction results for $\|\varepsilon_{w,h}\|_\infty$ and $\|\sigma_{w,h}\|_\infty$ obtained on the finite element meshes $\mathbb{K}_{h,i}$. From Table 7, we observe that the maximum reconstructed $\|\varepsilon_{w,h}\|_\infty = 10$ is obtained in all tests, which is close to the exact value $\|\varepsilon_w\|_\infty = 9$. However, obtaining an accurate contrast for $\|\sigma_{w,h}\|_\infty$ is more challenging.

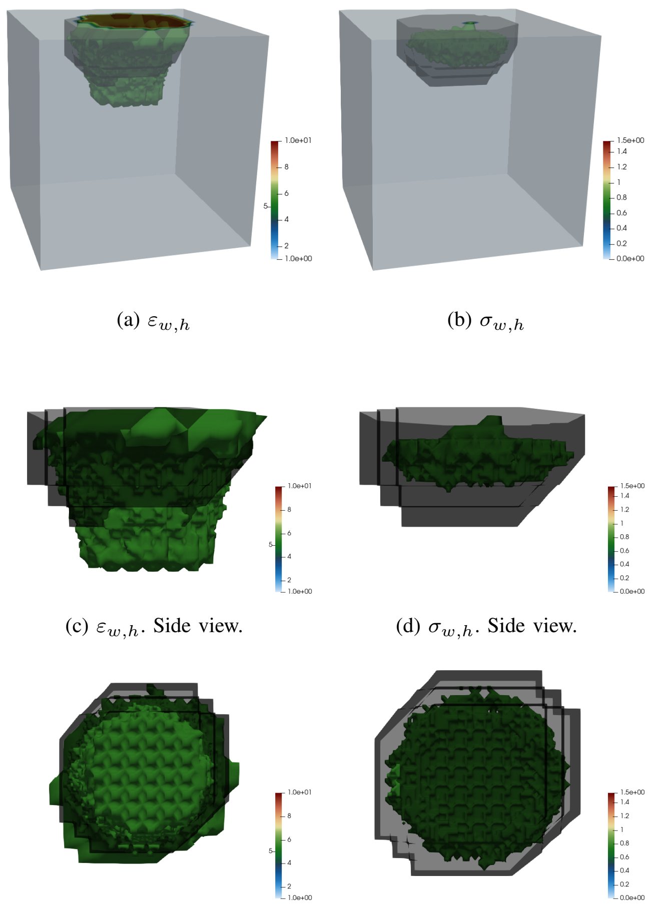

(a) $\varepsilon_{w,h}$ (b) $\sigma_{w,h}$

(c) $\varepsilon_{w,h}$. Side view. (d) $\sigma_{w,h}$. Side view.

(e) $\varepsilon_{w,h}$. Top view. (f) $\sigma_{w,h}$. Top view.

FIGURE 17: Test 5. Generated isosurfaces of the reconstructed solutions of $\varepsilon_{w,h}$ and $\sigma_{w,h}$ on $\mathbb{K}_{h,4}$ in a non-homogeneous medium using preprocessed and calibrated data, with initial values $\varepsilon_w^0 = 1$ and $\sigma_w^0 = 0$. The isosurfaces of the reference solutions are displayed in opaque dark gray.

TABLE 7: Summary of the final reconstruction results for $\|\varepsilon_{w,h}\|_\infty$ and $\|\sigma_{w,h}\|_\infty$ obtained on the finite element meshes $\mathbb{K}_{h,i}$ at 6 GHz. Here, i denotes the number of mesh refinements.

	Test 1 $\mathbb{K}_{h,7}$	Test 2 $\mathbb{K}_{h,4}$	Test 3 $\mathbb{K}_{h,5}$	Test 4 $\mathbb{K}_{h,4}$	Test 5 $\mathbb{K}_{h,4}$
$\|\varepsilon_w\|_\infty$	9	9	9	9	9
$\|\varepsilon_{w,h}\|_\infty$	10	10	10	10	10
$\|\sigma_w\|_\infty$	1.2	1.2	0.12	0.12	0.12
$\|\sigma_{w,h}\|_\infty$	1.29	0.88	2.0	0.21	1.54
$e_{\varepsilon_w} = \frac{\|\varepsilon_w - \varepsilon_{w,h}\|_\infty}{\|\varepsilon_w\|_\infty}$	0.11	0.11	0.11	0.11	0.11
$e_{\sigma_w} = \frac{\|\sigma_w - \sigma_{w,h}\|_\infty}{\|\sigma_w\|_\infty}$	0.08	0.27	15.7	0.75	11.8
comp. time (minutes)	14	7	10	7	7

The smallest relative errors $e_{\varepsilon_w} = \frac{\|\varepsilon_w - \varepsilon_{w,h}\|_\infty}{\|\varepsilon_w\|_\infty}$ and $e_{\sigma_w} = \frac{\|\sigma_w - \sigma_{w,h}\|_\infty}{\|\sigma_w\|_\infty}$ were obtained in Test 1 and 2 corresponding to the reconstruction of MM in a homogeneous domain.

Let us analyze the results of Tests 3, 4 and 5 which correspond to the reconstruction of MM in skin. We note that in these tests, we use a different reference value of $\|\sigma_w\|_\infty = 0.12$ than in Tests 1 and 2, in order to examine the influence of $\|\sigma_w\|_\infty$ on the reconstruction results. Reconstruction results for the dielectric properties of MM in skin with $\|\sigma_w\|_\infty = 1.2$ will be reported in future work. Tests 3, 4 and 5 show a small relative error e_{ε_w} in the reconstruction of ε_w but a relatively large error e_{σ_w} in the reconstruction of σ_w. We note that the relative error $e_{\varepsilon_w} = 0.11$ is close to the noise level 10% introduced into the observation data, which is consistent with the theory of inverse problems. The smallest relative errors $e_{\varepsilon_w} = 0.11$ and $e_{\sigma_w} = 0.75$ are obtained in Test 4 where the reconstructions were performed using calibrated and embedded data. Tests 3 and 5 exhibit very large relative errors in e_{σ_w} and should therefore be omitted from further testing when the objective is to reconstruct $\|\varepsilon_w\|_\infty$ and $\|\sigma_w\|_\infty$. However, if the interest lies only in reconstructing $\|\varepsilon_w\|_\infty$ and the shape of MM, these tests also yield good results.

To improve the reconstruction results for MM in skin in terms of the maximum contrast for $\sigma_{w,h}$, it would be necessary to use a different initial guess for σ_w^0 or to select a different step size in the CGA for $\sigma_{w,h}$. This leaves room for further investigation and for improvement of the reconstruction results in terms of the maximum contrast of $\sigma_{w,h}$.

However, all reconstructions of $\|\varepsilon_{w,h}\|_\infty$ show good recovery of the geometric properties of the MM in the skin, including its depth. The depth is not correctly reconstructed on the initial coarse mesh, and further mesh refinements are required. We also note that the smoothing procedure on the refined meshes allows us to obtain an accurate estimate of the melanoma depth. This can be explained by the fact that we smooth the obtained reconstructions over neighboring elements, which are locally refined precisely in regions where the maximum values of the dielectric permittivity and conductivity are computed. As a result, the smoothed reconstructed functions provide improved values for computing new reconstructions in the subsequent iteration of the ACGA.

Table 7 also presents the approximate computational times, in minutes, for all five tests. All computations were implemented efficiently in the WavES software package [40] and executed on a workstation at our home institution running Devuan GNU/Linux 4 (Chimaera). We observe that the reconstructions in Tests 2, 4, and 5 converged on meshes refined four times and required approximately 7 minutes of computational time. The reconstruction in Test 1 converged on a mesh refined seven times and took 14 minutes, while Test 3 converged on a mesh refined five times and required 10 minutes. We note that, in all tests, the reported times include not only the computational time but also the time required to export results for visualization in ParaView and GiD.

Overall, the results indicate that all computations were performed efficiently, suggesting that the reconstruction of dielectric properties can be achieved within minutes and highlighting the potential of the ACGA for real-time applications.

VI. CONCLUSION

The primary goal of this article is to develop efficient and reliable adaptive algorithms for reconstructing the weighted relative dielectric permittivity and weighted conductivity of a given domain. Using Maxwell's equations, an optimization-based approach was applied to simulated time-dependent backscattered electric field data. The resulting reconstructions show accurate localization, depth estimation, and recovery of the maximum values corresponding to the weighted dielectric properties of MM tissue as the mesh is refined using the ACGA.

The method proved successful, both quantitatively and qualitatively, for both homogeneous and non-homogeneous domains. The CIP was formulated using Maxwell's equations and the regularized Tikhonov functional was minimized via a Lagrangian approach. The resulting optimization problem was solved using an ACGA. To handle the solution of the associated partial differential equations, a domain decomposition method of [5] was applied. The authors of [5] demonstrated the effectiveness of this approach for reconstructing the dielectric permittivity of real breast phantoms from the database [38] for known conductivity, further supporting the method's applicability.

Our computational results demonstrate that the ACGA can reconstruct the maximum values of the weighted relative dielectric permittivity of MM tissue, both in a homogeneous domain and in skin, while also recovering its depth and shape once local mesh refinement is applied. The reconstruction results for MM in skin can still be improved with respect to the maximum contrast of σ_w. This may be achieved by using a different initial guess for σ_w^0 or by selecting a different step size in the CGA for σ_w.

Our computational results also indicate that all computations were performed efficiently, suggesting that the reconstruction of dielectric properties can be achieved within minutes and highlighting the potential of the ACGA for real-time applications.

Nevertheless, further research is required before the method can be developed into a robust tool for clinical applications. It was shown in [20] that MM tends to grow in cone-like shapes. In [27], such geometries were used and corresponding finite element meshes were produced. Future studies could incorporate the finite element geometries presented in [27] to improve the biological realism of the simulations.

REFERENCES

[1] O. Abuzaghleh, B. D. Barkana, and M. Faezipour, "Noninvasive Real-Time Automated Skin Lesion Analysis System for Melanoma Early Detection and Prevention," *IEEE J. Trans. Eng. Health Med.*, vol. 2, pp. 1–12, April 2015, DOI. 10.1109./*JTEHM*.2015.2419612.

[2] A. B. Bakushinsk, and M. Y. Kokurin, *Iterative Methods for Approximate Solution of Inverse Problems*. Dordrecht, Netherlands: Springer, 2004.

[3] L. Beilina, "Energy estimates and numerical verification of the stabilized Domain Decomposition Finite Element/Finite Difference approach for time-dependent Maxwell's system," *CEJM*, vol. 11, no. 4, pp. 702–733, Jan. 2013, DOI. 10.2478/*s*11533-013-0202-3.

[4] L. Beilina, A. Eriksson, and N. Neittaanmäki, "Frequency inversion method and device for malignant melanoma detection using RF/microwaves," in *ICEAA*, Lisbon, Portugal, 2024, pp. *794–799.*

[5] L. Beilina, and E. Lindström, "An Adaptive Finite Element/Finite Difference Domain Decomposition Method for Applications in Microwave Imaging," *Electronics*, vol. 11, no. 9, April 2022, DOI. 10.3390/*electronics*11091359.

[6] L. Beilina, and E. Lindström, "A Posteriori Error Estimates and Adaptive Error Control for Permittivity Reconstruction in Conductive Media," in *Gas Dynamics with Applications in Industry and Life Sciences*. Cham, Switzerland: Springer, 2023, pp. *117–141.*

[7] L. Beilina, and V. Ruas, "Explicit P1 Finite Element Solution of the Maxwell-Wave Equation Coupling Problem with Absorbing b. c.," *Mathematics*, vol. 12, no. 7, March 2024, DOI. 10.3390./*math*12070936.

[8] J. Boparai, R. Tchinov, O. Miller, Y. Jallouli, and M. Popović, "Models of Melanoma Growth for Assessment of Microwave-Based Diagnostic Tools," *IEEE J. Electromagn., RF, Microw. Med. Biol.*, vol. 8, no. 3, pp. 305–315, Sept. 2024, DOI. 10.1109./*JERM*.2024.3430315.

[9] S. C. Brenner, and L. R. Scott, *The Mathematical Theory of Finite Element Methods, 3*rd ed. New York, NY, USA: Springer, 2008.

[10] A. E. Bulyshev, A. E. Souvorov, S. Yu Semenov, V. G. Posukh, and Y. E. Sizov, "Three-dimensional vector microwave tomography: theory and computational experiments," *Inv. Prob.*, vol. 20, no. 4, pp. 1239–1259, June 2004, DOI. 10.1088/0266-5611/20/4/013.

[11] W. C. Chew, and Y. M. Wang, "Reconstruction of two-dimensional permittivity distribution using the distorted Born iterative method," *IEEE Trans. Med. Imag.*, vol. 9, no. 2, pp. 218–225, June 1990, DOI. 10.1109/42.56334.

[12] E. C. Fear, J. Bourqui, C. Curtis, D. Mew, B. Docktor, and C. Romano, "Microwave Breast Imaging With a Monostatic Radar-Based System: A Study of Application to Patients," *IEEE Trans. Microw. Theory Techn.*, vol. 61, no. 5, pp. 2119–2128, May 2013, DOI. 10.1109.*TMTT*.2013.2255884.

[13] J. E. Gershenwald, R. A. Scolyer, K. R. Hess, V. K. Sondak, G. V. Long, M. I. Ross, *et al.*, "Melanoma staging: Evidence-based changes in the American Joint Committee on Cancer eighth edition cancer staging manual," *CA: A Cancer J. Clinicians*, vol. 67, no. 6, pp. 472–492, Oct. 2017, DOI. 10.3322.*caac*.21409.

[14] T. M. Grzegorczyk, P. M. Meaney, P. A. Kaufman, R. M. diFlorio-Alexander, and K. D. Paulsen, "Fast 3-D Tomographic Microwave Imaging for Breast Cancer Detection," *IEEE Trans. Med. Imag.*, vol. 31, no. 8, pp. 1584–1592, Aug. 2012, DOI. 10.1109.*TMI*.2012.2197218.

[15] J. Hadamard, *Lectures on Cauchy's Problem in Linear Partial Differential Equations*. London, UK, Humphrey Milford, 1923.

[16] M. Haynes, and M. Moghaddam, "Vector Green's function for S-parameter measurements of the electromagnetic volume integral equation," *IEEE Trans. Antennas Propag.*, vol. 60, no. 3, pp. 1400–1413, March 2012, DOI. 10.1109.*TAP*.2011.2180324.

[17] M. Haynes, J. Stang, and M. Moghaddam, "Real-time Microwave Imaging of Differential Temperature for Thermal Therapy Monitoring," *IEEE Trans. Biomed. Eng.*, vol. 61, no. 6, pp. 1787–1797, June 2014, DOI. 10.1109.*TBME*.2014.2307072.

[18] T. Henriksson, *et al.*, "Clinical trials of a multistatic UWB radar for breast imaging," in *LAPC*, Loughborough, UK, 2011, pp. *1–4.*

[19] N. Joachimowicz, C. Pichot, and J. P. Hugonin, "Inverse scattering: an iterative numerical method for electromagnetic imaging," *IEEE Trans. Antennas Propag.*, vol. 39, no. 12, pp. 1742–1753, Dec. 1991, DOI. 10.1109/8.121595.

[20] W. T. Joines, Y. Zhang, C. Li, and R. L. Jirtle, "The measured electrical properties of normal and malignant human tissues from 50 to 900 MHz," *Med. Phys.*, vol. 21, no. 4, pp. 547–550, April 1994, DOI. 10.1118./1.597312.

[21] W. C. Khor, H. Wang, M. E. Bialkowski, A. Abbosh, and N. Seman, "An Experimental and Theoretical Investigation into Capabilities of a UWB Microwave Imaging Radar System to Detect Breast Cancer," in *EUROCON*, Warsaw, Poland, 2007, pp. *771–776.*

[22] M. Klemm, I. J. Craddock, J. A. Leendertz, A. Preece, and R. Benjamin, "Radar-Based Breast Cancer Detection Using a Hemispherical Antenna Array—Experimental Results," *IEEE Trans. Antennas Propag.*, vol. 57, no. 6, pp. 1692–1704, June 2009, DOI. 10.1109.*TAP*.2009.2019856.

[23] M. Křížek, and P. Neittaanmäki, *Finite Element Approximation of Variational Problems and Applications*. Harlow, UK: Longman Scientific & Technical, 1990.

[24] G. Kyhn, E. Lindström, and L. Beilina, "Reconstructing the Dielectric Properties of Melanoma in 3D Using Real-Life Melanoma Model," in *ICEAA*, Palermo, Italy, 2025, pp. *454–459.*

[25] E. Lindström, and L. Beilina, "A hybrid finite element/finite difference method for reconstruction of dielectric properties of conductive objects," in *ICEAA*, Lisbon, Portugal, 2024, pp. *788–793.*

[26] E. Lindström, and L. Beilina, "L. Energy norm error estimates and convergence analysis for a stabilized Maxwell's equations in conductive media," in *Appl. Math*, vol 69, pp. *415–436.* May 2024, DOI. 10.21136./*AM*.2024.0248-23.

[27] E. Lindström, and L. Beilina, "Finite Element 3D Models of Melanoma Growth and Time-Dependent Backscattered Data for Dielectric Properties of Melanoma at 6 GHz," in *ICEAA*, Palermo, Italy, 2025, pp. *442–448.*

[28] J. L. Mueller, and S. Siltanen, *Linear and Nonlinear Inverse Problems with Practical Applications*. Philadelphia, PA, USA: SIAM, 2012.

[29] K. D. Paulsen, and D. R. Lynch, "Elimination of vector parasites in finite element Maxwell solutions," *IEEE Trans. Microw. Theory Techn.*, vol. 39, no. 3, pp. 395–404, March 1991, DOI. 10.1109/22.75280.

[30] S. P. Poplack, T. D. Tosteson, W. A. Wells, B. W. Pogue, P. M. Meaney, A. Hartov, *et al.*, "Electromagnetic Breast Imaging: Results of a Pilot Study in Women with Abnormal Mammograms," *Radioligy*, vol. 243, no. 2, May 2007, DOI. 10.1148.*radiol*.2432060286.

[31] D. S. Rigel, and J. A. Carucci, "Malignant melanoma: Prevention, early detection, and treatment in the 21st century," *CA: A Cancer Journal for Clinicians*, vol. 50, no. 4, pp. 215–236, July 2000, DOI. 10.3322/*canjclin*.50.4.215.

[32] V. G. Romanov, and M. V. Klibanov, "Can a single scalar second order PDE govern well the propagation of the electric wave field in a heterogeneous 3D medium?," *J. Inv. Ill-posed Prob.*, vol. 30, no. 4, pp. 595–611, April 2022, DOI. 10.1515.*jiip*-2021-0085.

[33] S. Semenov, "Microwave tomography: review of the progress towards clinical applications," *Philos. Trans. A Math. Phys. Eng. Sci.*, vol. 367, no. 1900, pp. 3021–3042, Aug. 2009, DOI. 10.1098.*rsta*.2009.0092.

[34] N. T. Thành, L. Beilina, M. V. Klibanov, and M. A. Fiddy, "Reconstruction of the Refractive Index from Experimental Backscattering Data Using a Globally Convergent Inverse Method," *SIAM J. Sci. Comp.*, vol. 36, no. 3, pp. B273–B293, Jan. 2014, DOI. 10.1137/130924962.

[35] N. T. Thành, L. Beilina, M. V. Klibanov, and M. A. Fiddy, "Imaging of Buried Objects from Experimental Backscattering Time-Dependent Measurements Using a Globally Convergent Inverse Algorithm," *SIAM J. Imag. Sci.*, vol. 8, no. 1, pp. 757–786, Jan. 2015, DOI. 10.1137/140972469.

[36] L. A. Torre, F. Bray, R. L. Siegel, J. Ferlay, J. Lortet-Tieulent, and A. Jemal, "Global cancer statistics, 2012," *CA: A Cancer Journal for Clinicians*, vol. 65, no. 2, pp. 87–108, Feb. 2012, DOI. 10.3322./*caac*.21262.

[37] X. Zeng, A. Fhager, Z. He, M. Persson, P. Linner, and H. Zirath, "Development of a Time Domain Microwave System for Medical Diagnostics," *IEEE Trans. Instrum. Meas.*, vol. 63, no. 12, pp. 2931–2939, Dec. 2014, DOI. 10.1109.*TIM*.2014.2326277.

[38] Database of 3D Grid-Based Numerical Breast Phantoms for use in Computational Electromagnetics Simulations. [Online]. Available: https://uwcem.ece.wisc.edu/MRIdatabase

[39] PETSc, software package. [Online]. Available: https://petsc.org/

[40] WaveES, software package. [Online]. Available: https://waves24.com/

[41] Paraview, open source visualization application. [Online]. Available: https://www.paraview.org/

[42] GiD, pre- and post-processing visualization application. [Online]. Available: https://www.gidsimulation.com/

Georg Kyhn was born in Copenhagen, Denmark, in 1998. He received the M.S. degree in mathematics from Gothenburg University, Gothenburg, Sweden, in 2025. Since 2025 he is a PhD student at the Department of Mathematical Sciences, Gothenburg University and Chalmers University of Technology, Gothenburg, Sweden.

His main research interests are in adaptive finite-element methods and in inverse problems for partial differential equations.

Larisa Beilina was born in Jelgava, Latvia, in 1970. She received the M.S. degree in mathematics from the University of Latvia, Riga, in 1994, and the Ph.D. degree in mathematics from Chalmers University of Technology, Gothenburg, Sweden, in 2003. She was a Postdoctoral Fellow at the University of Basel, Switzerland, from 2003 to 2005, and at the Norwegian University of Science and Technology (NTNU), Trondheim, Norway, from 2007 to 2008. Since 2009, she has been affiliated with the Department of Mathematical Sciences at Chalmers University of Technology as well as with the University of Gothenburg, Gothenburg, Sweden. Since 2018, she has held the position of Full Professor of Applied Mathematics at the same department.

Her main research interests are in adaptive finite-element methods and in inverse problems for partial differential equations.